Available online at www.sciencedirect.com

ScienceDirect

Geochimica et Cosmochimica Acta 238 (2018) 477–495

Geochimica et Cosmochimica Acta

www.elsevier.com/locate/gca

Core-mantle fractionation of carbon in Earth and Mars: The effects of sulfur

Kyusei Tsuno *, Damanveer S. Grewal, Rajdeep Dasgupta

Department of Earth, Environmental and Planetary Sciences, Rice University, 6100 Main Street, MS 126, Houston, TX 77005, USA

Received 28 March 2018; accepted in revised form 3 July 2018; available online 18 July 2018

Abstract

Constraining carbon (C) fractionation between silicate magma ocean (MO) and core-forming alloy liquid during early differentiation is essential to understand the origin and early distribution of C between reservoirs such as the crust-atmosphere, mantle, and core of Earth and other terrestrial planets. Yet experimental data at high pressure (P)-temperature (T) on the effect of other light elements such as sulfur (S) in alloy liquid on alloy-silicate partitioning of C and C solubility in Fe-alloy compositions relevant for core formation is lacking. Here we have performed multi-anvil experiments at 6–13 GPa and 1800–2000 °C to examine the effects of S and Ni on the solubility limit of C in Fe-rich alloy liquid as well as partitioning behavior of C between alloy liquid and silicate melt ($D_C^{alloy/silicate}$). The results show that C solubility in the alloy liquid as well as $D_C^{alloy/silicate}$ decreases with increasing in S content in the alloy liquid. Empirical regression on C solubility in alloy liquid using our new experimental data and previous experiments demonstrates that C solubility significantly increases with increasing temperature, whereas unlike in S-poor or S-free alloy compositions, there is no discernible effect of Ni on C solubility in S-rich alloy liquid.

Our modelling results confirm previous findings that in order to satisfy the C budget of BSE, the bulk Earth C undergoing alloy-silicate fractionation needs to be as high as those of CI-type carbonaceous chondrite, i.e., not leaving any room for volatility-induced loss of carbon during accretion. For Mars, on the other hand, an average single-stage core formation at relatively oxidized conditions (1.0 log unit below IW buffer) with 10–16 wt% S in the core could yield a Martian mantle with a C budget similar to that of Earth's BSE for a bulk C content of ~0.25–0.9 wt%. For the scenario where C was delivered to the proto-Earth by a S-rich differentiated impactor at a later stage, our model calculations predict that bulk C content in the impactor can be as low as ~0.5 wt% for an impactor mass that lies between 9 and 20% of present day Earth's mass. This value is much higher than 0.05–0.1 wt% bulk C in the impactor predicted by Li et al. (Li Y., Dasgupta R., Tsuno K., Monteleone B., and Shimizu N. (2016) Carbon and sulfur budget of the silicate Earth explained by accretion of differentiated planetary embryos. *Nat. Geosci.* **9**, 781–785) because C-solubility limit of 0.3 wt% in a S-rich alloy predicted by their models is significantly lower than the experimentally derived C-solubility of ~1.6 wt% for the relevant S-content in the core of the impactor.

Keywords: Carbon; Sulfur; Early Earth differentiation; Core formation; Magma ocean; Giant impact; Planet formation

1. INTRODUCTION

Deep cycling of major volatile elements such as carbon (C) and sulfur (S) in Earth and other terrestrial planets plays a crucial role in the dynamics of planetary interior processes such as partial melting (e.g., Wyllie and Huang, 1975; Eggler, 1978; Mallik and Dasgupta, 2014; Namur et al., 2016; Dasgupta, 2018) and mobilization of important trace metals (e.g., Lee et al., 2012; Li and Audétat, 2012; Kiseeva and Wood, 2013; Ding and Dasgupta, 2017) as well as long term evolution of planetary climates and

* Corresponding author.
E-mail address: Kyusei.Tsuno@rice.edu (K. Tsuno).

https://doi.org/10.1016/j.gca.2018.07.010
0016-7037/

habitability (e.g., Halevy et al., 2007; Zahnle et al., 2007; Dasgupta, 2013; Ding et al., 2015; Duncan and Dasgupta, 2017). The present-day distribution of carbon among the main terrestrial reservoirs, i.e., ocean-atmosphere, crust, mantle and core could have been set by early planetary accretion and differentiation processes (e.g., Kuramoto and Matsui, 1996; Kuramoto, 1997; Dasgupta, 2013). However, the delivery mechanism of C along with the role of core-mantle differentiation and magma ocean (MO) degassing in setting up the C budget of key terrestrial reservoirs are not definitively known.

Core-mantle differentiation is one of the most efficient ways of establishing the initial elemental concentrations (Wood, 1993; Dasgupta et al., 2013; Chi et al., 2014; Li et al., 2015; Armstrong et al., 2015; Li et al., 2016a; Suer et al., 2017; Clesi et al., 2018) as well as isotopic compositions (Labidi et al., 2016; Li et al., 2016b) of key volatile elements in the silicate and metallic fractions of the rocky planets. It has been widely suggested that the Earth's interior is the largest reservoir of carbon, however, constraints on the relative distribution of carbon between the Earth's mantle and core have only begun to emerge in recent years (Dasgupta et al., 2013; Chi et al., 2014; Armstrong et al., 2015; Li et al., 2015, 2016a). Based on the analysis of mantle-derived magma and fluids, Earth's mantle is thought to be one of the largest reservoirs of carbon (Hirschmann and Dasgupta, 2009; Dasgupta and Hirschmann, 2010; Marty, 2012; Kelemen and Manning, 2015; Michael and Graham, 2015; Le Voyer et al., 2017). Alternatively, Earth's core could be an even larger reservoir of carbon owing to its high solubility in Fe-Ni alloy liquid (e.g., Hirayama et al., 1993; Dasgupta and Walker, 2008; Nakajima et al., 2009; Fei and Brosh, 2014). Much less is known about the budget and relative distribution of C in other inner Solar System planets such as Mars (McCubbin et al., 2012, 2010; Gross et al., 2013; Stanley et al., 2014; Chi et al., 2014). Therefore, to constrain the initial budget and distribution of C in the planetary interiors set by early differentiation processes like core formation, it is important to quantify solubility limit of C in Fe-Ni alloy and partitioning behavior of C between the Fe-Ni alloy liquid and silicate melt under relevant planetary MO conditions. One critical variable that may affect the C fractionation during core-mantle equilibration is the other non-metal content in the alloy, light element such as sulfur.

The effect of S content in Fe-Ni alloys on the solubility limit of C has been systematically constrained via high temperature experiments at ambient pressure (Wang et al., 1991; Bouchard and Bale, 1995; Tsymbulov and Tsemekhman, 2001). These 1-atmosphere experimental studies, conducted over temperature range of 1200–1600 °C, demonstrated that C solubility in Fe-rich alloy melt decreases strongly with increasing S content of the alloy (Fig. 1a). However, because core formation in terrestrial planets occurred through much higher *P-T* processes, the well-established 1-atm systematics need to be extended to higher *P-T*. The majority of high pressure (≥1 GPa) data for C-solubility limit in S-bearing Fe-rich alloys either lies in a narrow range of S in the alloy (0–20 wt%) (Wood, 1993; Dasgupta et al., 2009; Buono et al., 2013; Deng et al., 2013), or extremely Ni-rich alloys (>15 wt%) that are not relevant for core forming alloy at least for Earth (Tsuno and Dasgupta, 2015; Zhang et al., 2018); therefore, a systematic enquiry into C-solubility limit in S-rich, Fe-alloys with relevant Ni contents is required at high pressures and temperatures approaching magma ocean conditions. Similarly, previous experimental studies on measurement of $D_C^{alloy/silicate}$(C partitioning between alloy liquid and silicate melt) have also focused on S-poor alloys (0–5 wt%) (Fig. 1b) (Dasgupta et al., 2013; Chi et al., 2014; Stanley et al., 2014; Li et al., 2015; Armstrong et al., 2015; Li et al., 2016a; Dalou et al., 2017; Duncan et al., 2017)

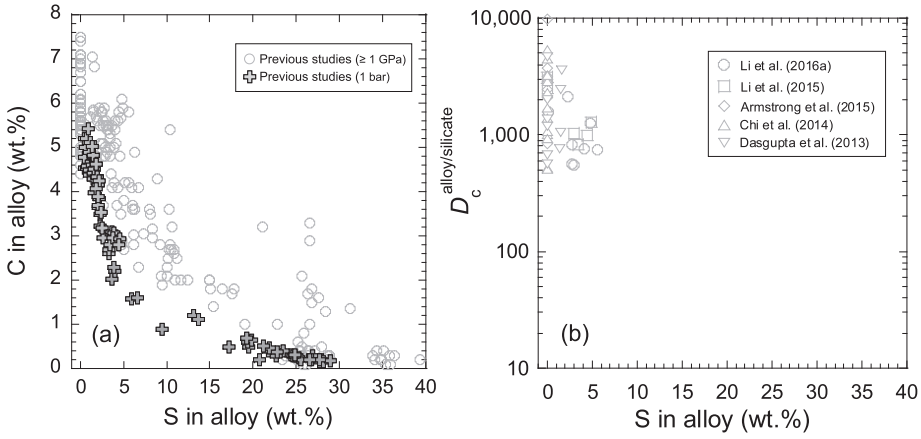

Fig. 1. (a) Previous studies on C solubility (in wt.%) in the S-bearing Fe-Ni alloy as a function of S content at ambient pressure (Wang et al., 1991, Bouchard and Bales, 1995 and Tsymbulov et al., 2001) and at high pressures and Ni content in the alloy relevant for planetary core compositions (≤20 wt%) (Dasgupta et al., 2009; Dasgupta et al., 2013; Deng et al., 2013; Chi et al., 2014; Boujibar et al., 2014; Armstrong et al., 2015; Li et al., 2016a, 2015; Zhang et al., 2018). High pressure data from the study of Tsuno and Dasgupta (2015) and Zhang et al. (2015) and most data from the study of Zhang et al. (2018) with ≥20 wt% Ni have not been plotted as such compositions are not of direct relevance to planetary cores such as those of Earth and Mars. (b) Previous studies on $D_C^{alloy/silicate}$ as a function of S content in the alloy liquid (Dasgupta et al., 2013; Chi et al., 2014; Armstrong et al., 2015; Li et al., 2015; Li et al., 2016a). The plots show that high pressure C solubility data for core-relevant Fe-Ni alloy liquid that is reach in sulfur as well as $D_C^{alloy/silicate}$ for S-rich Fe-Ni alloy liquid are lacking.

chiefly because of the fact that the geochemical constraints on the S-content of Earth's core is S-poor (~2 wt%) (Allègre et al., 1995; McDonough, 2013; Palme and O'Neill, 2013; Badro et al., 2015). However, recent planetary accretion models have predicted that material of varying compositions may have merged with the growing proto planets at different stages of accretion (O'Neill, 1991; Rubie et al., 2011; Siebert et al., 2013; Rubie et al., 2015; Badro et al., 2015). Therefore, it is conceivable that the early proto-Earth was accreted from volatile depleted material followed by late stage accretion of planetary embryos that were more S-rich compared to the final composition of the Earth. Many studies have considered the role of late stage addition of S-rich differentiated bodies in accretion models relevant for Earth (Wood, 2008; Wood et al., 2014; Wohlers and Wood, 2015, 2017). A recent study has postulated that accretion of S-rich differentiated impactors to a volatile depleted proto-Earth can also explain the C budget of the bulk silicate Earth (Li et al., 2016a). However, none of the experimental studies till now have systematically constrained the effect of S in the alloy liquid (up to ~36 wt%) on C solubility and partitioning of C between Fe-rich alloy and silicate melts. Li et al. (2016a) obtained C solubility for S-rich alloy liquid under deep planetary magma ocean conditions by approximating C solubility data from low pressures and temperatures while carbon partitioning for S-rich alloy liquid was calculated using the extrapolated C partitioning data for S-poor alloy.

While considering the potential difference in composition of the accreting material and the final composition of the Earth, Ni content of the alloy is another compositional parameter of importance. The presence of Ni affects the physical and chemical properties of the alloy liquid, including the C solubility (Tsuno and Dasgupta, 2015; Zhang et al., 2018). Previous alloy liquid-silicate melt partitioning experiments typically employed alloys with ~5–10 wt% Ni in accordance with Ni content of present-day Earth's core (~5 wt%; e.g., Allègre et al., 1995; McDonough, 2013). However, if iron meteorites, which include Fe-rich metal with ~25 wt% Ni, are representative of cores of differentiated terrestrial bodies (Bottke et al., 2006), then Ni content of the impactor's core can be higher than the generally accepted value of the Earth's core.

In order to understand the role of S-rich Fe-Ni alloy liquid on carbon distribution between the metal and silicate fraction of various planetary bodies during the early differentiation of terrestrial planets, we performed experiments to systematically investigate (1) the effects of S and Ni on solubility limit of carbon in Fe-rich alloy liquid and (2) partitioning behavior of carbon between S-rich alloy liquid and silicate melt at pressures of 6–13 GPa and temperature of 1800–2000 °C. Application of the experimental results from this study confirm that in order to explain the C budget of BSE via single-stage equilibrium core formation, nearly carbonaceous chondrite-like abundance of carbon in the bulk system is required. However, late stage delivery of C-S in accordance with Li et al. (2016a, 2016b), suggests that the merger of a relatively oxidized, S-rich differentiated planetary embryo to a reduced, growing Earth can satisfy the C budget and C/S ratio in the bulk silicate Earth (BSE) for an impactor bulk C-content as low as ~0.5 wt%. The proposed bulk C content of the impactor is, however, distinctly higher than the predicted bulk C content of 0.05–0.1 wt% in the impactor by Li et al. (2016a). Additionally, we also show that relatively C-poor building blocks (~0.25–0.9 wt%) can deliver modest amount of C into the Martian mantle for an averaged single-stage core formation.

2. METHODS

2.1. Starting mixes

For experiments conducted at 6 GPa, nine sets of starting materials composed of mixtures of natural BCR-2 basalt and sulfide alloy (2:1 in weight ratio) were prepared (Tables 1 and 2). Natural BCR basalt was fired using a CO–CO_2 Deltech gas mixing furnace at 1000 °C for 20 h and under ~1–2 log units below QFM (quartz-fayalite-magnetite) buffer to minimize water contamination and the presence of Fe^{3+} in the starting mixes. The compositions of nine different S-rich alloy mixtures, that vary between 0 and 15 wt% Ni and 10–36 wt% S (Table 1), were prepared by mixing reagent grades Fe and Ni metals, and FeS and/or natural pyrite (all obtained from Alfa Aesar). Graphite capsules were the source of carbon in our 6 GPa experiments. For 10 and 13 GPa experiments, 8–15 wt% of glassy carbon (Alfa Aesar) was homogeneously mixed with the alloy–silicate mixture used for 6 GPa experiments. All of the eighteen starting materials (Table 2) were then stored in a desiccator at room temperature. To further remove moisture, prior to performing experiments the starting mixes were placed in a 110 °C oven for ~4 h before loading into graphite (6 GPa) or MgO (10–13 GPa) capsules. For experiments at 10–13 GPa, the silicate fraction in the starting mixes was used to chiefly contain the alloy melt within the graphite capsule by largely preventing the alloy melt from percolating through the capsule, while for

Table 1
Chemical compositions of starting materials (in wt.%).

BCR-2	SiO_2	TiO_2	Al_2O_3	FeO*	MnO
	54.1	2.26	13.5	12.42	0.2
	CaO	MgO	Na_2O	K_2O	P_2O_5
	7.12	3.59	3.16	1.79	0.35
Alloy mix	Fe	Ni	S		
Fe-0Ni-10S	90	0	10		
Fe-0Ni-20S	80	0	20		
Fe-0Ni-36S	64	0	36		
Fe-5Ni-10S	85	5	10		
Fe-5Ni-20S	75	5	20		
Fe-5Ni-36S	59	5	36		
Fe-15Ni-10S	75	15	10		
Fe-15Ni-20S	65	15	20		
Fe-15Ni-36S	49	15	36		

BCR-2, a natural Columbia River Basalt, is USGS geochemical reference material. Before mixing with alloy mix, we fired silicate mix in gas-mixing furnace at 1000 °C under ~1–2 units below QFM buffer in order to remove excess water.

Table 2
Summary of experimental conditions, quench products, measured volatiles abundance, and carbon partitioning.

Run. No	P (GPa)	[a]T (°C)	[b]Duration (min)	[c]Starting materials	Capsule material	[d]fO_2 (ΔIW)	[e]fO_2 (ΔIW)	n	[f]C (ppm) (1-σ)	[f]H_2O (wt.%) (1-σ)	[g]NBO/T in SM	$D_S^{alloy/silicate}$ (1-σ)	$D_S^{alloy/silicate}$ (1-σ)	[h]SM texture
MA145-10S	6	1800	15	BCR-2 (67%) + Fe-0Ni-10S (33%)	Graphite	−1.34	−0.81	4	13(1)	0.24(0)	0.63	3493(289)	111(21)	Glass
MA145−20S	6	1800	15	BCR-2 (67%) + Fe-0Ni-20S (33%)	Graphite	−1.29	−1.23	3	14(0)	0.22(0)	0.58	1254(116)	179(29)	Glass
MA145-36S	6	1800	15	BCR-2 (67%) + Fe-0Ni-36S (33%)	Graphite	−1.04	−2.04			–	0.62	–	199(24)	Dendritic
MA142-10S	6	1800	15	BCR-2 (67%) + Fe-5Ni-10S (33%)	Graphite	−1.26	−0.68	4	15(1)	0.43(1)	0.64	2658(402)	117(15)	Glass
MA142-20S	6	1800	15	BCR-2 (67%) + Fe-5Ni-20S (33%)	Graphite	−1.17	−1.13	4	16(1)	0.39(1)	0.64	873(12)	197(21)	Glass
MA142-36S	6	1800	15	BCR-2 (67%) + Fe-5Ni-36S (33%)	Graphite	−1.03	−2.15		–	–	0.59	–	171(37)	Dendritic
MA144-10S	6	1800	15	BCR-2 (67%) + Fe-15Ni-10S (33%)	Graphite	−1.02	−0.44	3	13(1)	0.10(0)	0.72	2569(325)	124(38)	Glass
MA144-20S	6	1800	15	BCR-2 (67%) + Fe-15Ni-20S (33%)	Graphite	−0.86	−1.04		–	–	0.79	–	145(40)	Dendritic
MA144-36S	6	1800	15	BCR-2 (67%) + Fe-15Ni-36S (33%)	Graphite	−0.92	−1.89		–	–	0.57	–	179(22)	Dendritic
MA158-10S	6	2000	2	BCR-2 (67%) + Fe-0Ni-10S (33%)	Graphite	−1.42	−0.83	2	65(7)	0.35(0)	0.57	703(146)	61(18)	Glass
MA158-20S	6	2000	2	BCR-2 (67%) + Fe-0Ni-20S (33%)	Graphite	−1.67	−1.58	3	141(8)	0.60(2)	0.47	117(13)	54(6)	Glass
MA158-36S	6	2000	2	BCR-2 (67%) + Fe-0Ni-36S (33%)	Graphite	−1.51	−2.33		–	–	0.47	–	77(10)	Dendritic
MA152-10S	6	2000	3	BCR-2 (67%) + Fe-5Ni-10S (33%)	Graphite	−1.38	−0.78		–	–	0.59	–	57(10)	Dendritic
MA152-20S	6	2000	3	BCR-2 (67%) + Fe-5Ni-20S (33%)	Graphite	−1.27	−1.13	3	28(1)	0.53(1)	0.58	553(65)	98(20)	Glass
MA152-36S	6	2000	3	BCR-2 (67%) + Fe-5Ni-36S (33%)	Graphite	−0.96	−1.79		–	–	0.51	–	98(9)	Dendritic
MA160-10S	6	2000	2	BCR-2 (67%) + Fe-15Ni-10S (33%)	Graphite	−0.84	−0.37		–	–	0.85	–	60(8)	Dendritic
MA160-20S	6	2000	2	BCR-2 (67%) + Fe-15Ni-20S (33%)	Graphite	−0.68	−0.80	4	215(81)	0.96(0)	0.78	53(22)	66(11)	Glass
MA160-36S	6	2000	2	BCR-2 (67%) + Fe-15Ni-36S (33%)	Graphite	−0.95	−1.83		–	–	0.51	–	127(18)	Dendritic
MA173-10S	10	1800	15	BCR-2 (57%) + Fe-0Ni-10S (28%) + GC (15%)	MgO		–		–	–	–	–	–	Dendritic
MA173-20S	10	1800	15	BCR-2 (57%) + Fe-0Ni-20S (28%) + GC (15%)	MgO		–		–	–	–	–	–	Dendritic
MA173-36S	10	1800	15	BCR-2 (57%) + Fe-0Ni-36S (28%) + GC (15%)	MgO		–		–	–	–	–	–	Dendritic
MA168-10S	10	1800	15	BCR-2 (62%) + Fe-5Ni-10S (30%) + GC (8%)	MgO		–		–	–	–	–	–	Dendritic
MA168-20S	10	1800	15	BCR-2 (62%) + Fe-5Ni-20S (30%) + GC (8%)	MgO		–		–	–	–	–	–	Dendritic
MA168-36S	10	1800	15	BCR-2 (62%) + Fe-5Ni-36S (30%) + GC (8%)	MgO		–		–	–	–	–	–	Dendritic
MA169-10S	10	1800	15	BCR-2 (57%) + Fe-15Ni-10S (28%) + GC (15%)	MgO		–		–	–	–	–	–	Dendritic
MA169-20S	10	1800	15	BCR-2 (57%) + Fe-15Ni-20S (28%) + GC (15%)	MgO		–		–	–	–	–	–	Dendritic
MA169-36S	10	1800	15	BCR-2 (57%) + Fe-15Ni-36S (28%) + GC (15%)	MgO		–		–	–	–	–	–	Dendritic
MA174-10S	13	1800	15	BCR-2 (57%) + Fe-15Ni-10S (28%) + GC (15%)	MgO		–		–	–	–	–	–	Dendritic
MA174-20S	13	1800	15	BCR-2 (57%) + Fe-15Ni-20S (28%) + GC (15%)	MgO		–		–	–	–	–	–	Dendritic
MA174-36S	13	1800	15	BCR-2 (57%) + Fe-15Ni-36S (28%) + GC (15%)	MgO		–		–	–	–	–	–	Dendritic

n is the number of measurements via SIMS on silicate glasses to obtain the bulk C and H2O contents.
Errors, reported in parentheses, for bulk C and H2O contents are 1 − σ based on replicate SIMS analyses and are reported as the last digit cited. 13(1) should be read as 13 ± 1 ppm.
Errors, reported in parentheses, for alloy/silicate partition coefficients of C and S are propagated based on 1 − σ errors of C and S measurements in alloy and silicate melts.

[a] Sample temperature reported here is based on the temperature measured using type-C TC (1760 or 1960 °C) and determination of temperature gradient between the TC junction and sample area (~40 °C).

[b] The experiments were held at 900 °C for 15–27 h before raising to the target temperature in order to reduce the porosity of graphite and MgO capsules and prevent the leakage of silicate melt and alloy liquid.

[c] Mixture of BCR-2 basalt, Fe-Ni-S alloy (see Table 1), and glassy carbon (GC).

[d] fO_2 with respect to iron-wüstite buffer (ΔIW) calculated using ideal solution model and average composition of FeO in silicate and Fe in alloy melt.

[e] fO_2 with respect to iron-wüstite buffer (ΔIW) calculated using non-ideal solution model for both alloy and silicate melts (see text for details)

[f] Measured using SIMS.

[g] NBO/T = (2 × Total O)/T − 4, where T = Si + Ti + Al + Cr + P.

[h] Silicate melt (SM) texture: 'Glass' shows the presence of glass pool in silicate melt phase. 'Dendritic' denotes the melt pool composed of dendritic quenched crystals.

experiments at 6 GPa, the use of silicates provided the opportunity to obtain alloy-silicate partitioning information for carbon and sulfur.

2.2. Experimental techniques

Experiments were carried out using tungsten carbide cubes with 26 mm long edges and 8 mm truncation edge length (TEL) in a Walker-type multi-anvil device at the experimental petrology laboratory of Rice University. MgO octahedra with 14 mm edge lengths, cylindrical ZrO_2 thermal insulator and rhenium heater (Fig. 2a) were obtained from COMPRES (Consortium for Materials Properties Research in Earth Sciences). For 6 GPa experiments, the starting materials were placed in a 3–chamber graphite capsules (inset of Fig. 2a) while for 10–13 GPa experiments, we loaded basalt + alloy starting materials containing amorphous carbon (Table 2) in 3-chamber MgO capsules (Fig. 2a and b) in order to avoid polishing diamond capsules that resulted from graphite to diamond transformations at these high *P-T* experiments. Further, the inability to quench basaltic glasses at 10–13 GPa makes accurate quantification of C and H using SIMS difficult (Dasgupta et al., 2013; Chi et al., 2014). Therefore, for the 10–13 GPa experiments, we analyzed the alloy liquid phase only to determine C solubility limits.

The 14/8 multi-anvil assembly used in this study was calibrated at 1200 °C (Fig. 2c) by coesite–stishovite boundary in SiO_2 (Zhang et al., 1996; Ono et al., 2017), and chemical compositions of coexisting olivine and ringwoodite in $(Mg_{0.6}Fe_{0.4})_2SiO_4$ and olivine and wadsleyite in $(Mg_{0.9}Fe_{0.1})_2SiO_4$ (Frost and Dolejš, 2007). The thermal gradient in our 14/8 assembly was determined using the two-pyroxene thermometer of Nickel et al. (1985). Temperature difference between the thermocouple junction and the center of the sample area was found to be ~40 °C. Temperature was measured and controlled using a type C ($W_{95}Re_5/W_{74}Re_{26}$) thermocouple that was positioned directly above the capsule (Fig. 2a). Temperature for all the experiments was first increased to 900 °C and then kept at the same temperature for 15–27 h in order to reduce the porosity of the graphite and MgO capsules so that there is minimal leakage of both silicate melt and alloy liquid from the capsule. After sintering, the assembly was heated to the target temperature and kept there for 15 min for 1800 °C experiments and 2–3 min for 2000 °C experiments. All experiments were brought down to ≤200 °C within 10 s by switching off the electric power to the heater.

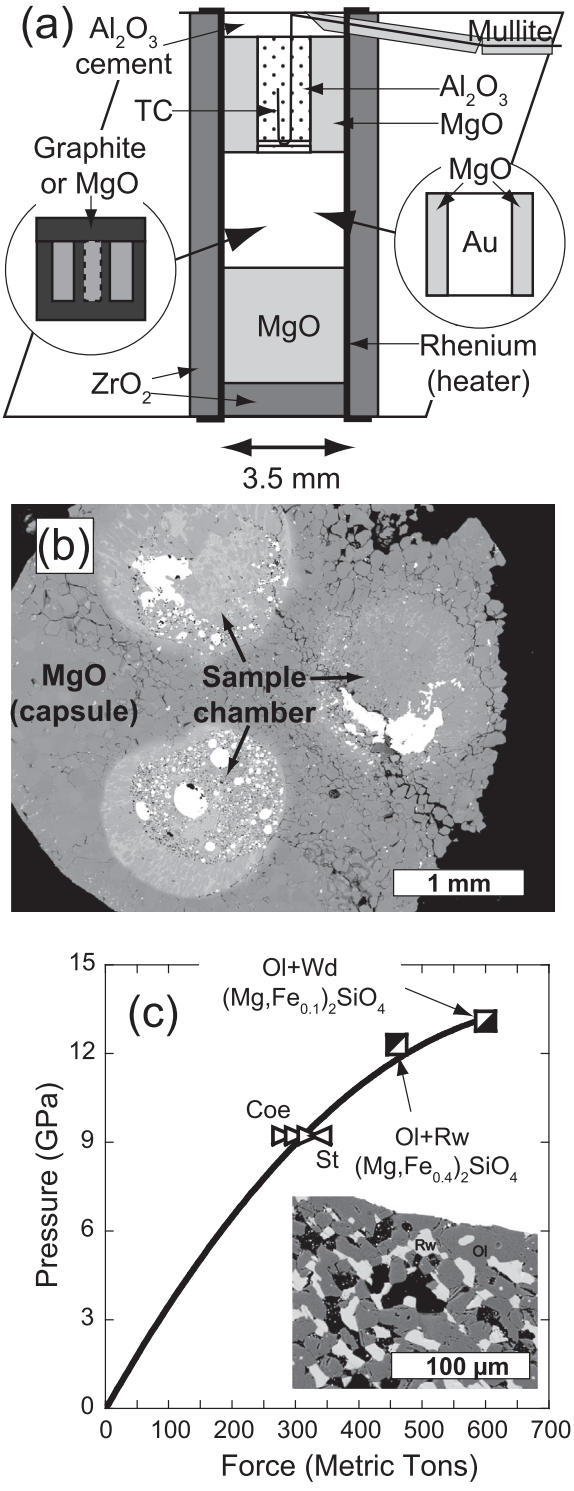

Fig. 2. (a) COMPRES 14/8 cell assembly used for this study, which consists of MgO octahedra with 14-mm edge lengths, cylindrical ZrO_2 insulator and sheet, rhenium foil heater, MgO spacer, Al_2O_3 tubing for placing type C thermocouple, and mullite tubing for insulating thermocouple from rhenium heater. The insets on the right and left show 3–chamber graphite or MgO capsule for C partitioning experiments and gold capsule with MgO ring for pressure calibration experiments. (b) Back-scattered electron image of experiment MA168 showing a 3-chamber MgO capsule that contained BRC-2 basalt + alloy materials which includes 10, 20 and 36 wt% S. (c) Pressure calibration curve for the 14/8 cell assembly for the 1100-ton multi anvil device at Rice University. The force–pressure relationship was calibrated at 1200 °C against coesite (Coe)–stishovite (St) transition in SiO_2 (Zhang et al., 1996; Ono et al., 2017), and the chemical compositions of coexisting olivine (Ol) and ringwoodite (Rw) in $(Mg,Fe_{0.4})_2SiO_4$ and olivine and wadsleyite (Wd) in $(Mg,Fe_{0.1})_2SiO_4$ (Frost and Dolejš, 2007). The fitted curve is described by P (GPa) = $(3.9494 \times 10^{-2}) \times F - (2.9477 \times 10^{-5}) \times F^2$ (metric tons).

2.3. Sample preparation and characterization

Recovered samples were polished laterally to observe 3-sample chambers simultaneously (Fig. 2b). The recovered products from 6 GPa experiments were mounted in Crystalbond™, ground using 1200-grit sand paper and polished with 0.3 μm aluminum slurry on a velvet cloth. The polished samples were soaked in acetone for at least 2 h for a couple of times to completely remove the Crystalbond™ and then coated using either carbon (for silicate melt analysis) or aluminum (for alloy analysis). After the completion of electron microprobe measurements, carbon or aluminum coating was removed and then the samples were mounted in indium, coated with gold, and analyzed using secondary ionization mass spectrometer (SIMS). The recovered products from 10 to 13 GPa were mounted in petropoxy, polished and coated using aluminum, and were analyzed using EPMA.

2.3.1. Electron microprobe analysis

We used a field emission gun electron microprobe analyzer (JEOL JXA-8530F Hyperprobe) at the Department of Earth, Environmental and Planetary Sciences of Rice University to analyze the major elements in quenched silicate and alloy melts. For analyzing silicate melt using a WDS mode, we used a beam diameter of 20 μm, 15 kV accelerating voltage, and 10 nA beam current. The standards used for calibration were a natural basaltic glass for Si, Al, Fe, Ca, Mg, and K, albite for Na, rutile for Ti, pyrite for S, pure Ni metal for Ni, apatite for P, and rhodonite for Mn. Counting times for K, Na, and P were 10 s for peak and 5 s for background while those for other elements were 20 s and 10 s. For determining C content of alloy liquids, we adopted the procedure from previous studies (e.g., Dasgupta and Walker, 2008; Sanloup et al., 2011; Buono et al., 2013; Tsuno and Dasgupta, 2015) with slight modifications described as follows. Both the experimental products and the analytical standards were coated with aluminum with thickness of 20 nm using SEMICORE SC2000 evaporator installed in Department of Electrical and Computer Engineering, Rice University. The standards used were pure Fe metal, pure Ni metal, pure Si metal, natural troilite for sulfur, synthetic stoichiometric cementite (Fe_3C) (Walker et al., 2013) for carbon, and natural magnetite for oxygen. WDS analysis of carbon was performed using a LDE2 crystal. To minimize hydrocarbon contamination during the C analysis in microprobe vacuum chamber, liquid nitrogen was supplied in cold-finger close to the stage. Counting time for carbon were 10 s for peak and 5 s for each background. We varied emission current to detect the optimum conditions for analyzing carbon in alloy liquids using LDE2 crystal at constant voltage of 12 kV and beam diameter of 20 μm. We obtained counts of C Kα peak and background signal of cementite in the range of 15–100 nA and confirmed that the peak/background for 50–100 nA is constant and slightly higher than for 15–20 nA. Analyses of pure Fe metal and natural troilite were performed to establish blank values for carbon to determine the amount of hydrocarbon contamination on the sample surface because the difference of hydrocarbon contamination between Fe metal and sulfide is critical for evaluating actual C solubility in the alloy liquid. We found that for the entire range of beam current explored (15–100 nA), the hydrocarbon contamination of troilite is constantly higher by ~0.25 wt% than the Fe metal standard (Supplementary fig. 1). This may be due to the thermal diffusivity of troilite being lower than that of Fe metal. We note that our observation of troilite yielding higher background C contamination is opposite to what was observed recently in Zhang et al. (2018). Taking into consideration various analytical caveats, we employed 50 nA beam current in this study. The experimental C content in the alloy liquid was estimated with the background correction for carbon varying linearly with alloy S content (Supplementary fig. 1).

Supplementary data associated with this article can be found, in the online version, at https://doi.org/10.1016/j.gca.2018.07.010.

2.3.2. Secondary ionization mass spectrometry (SIMS)

For analyzing carbon in silicate glasses, we used Cameca IMS 1280, a large-radius ion microprobe at Woods Hole Oceanographic Institution, following the protocol detailed in our previous publications (Dasgupta et al., 2013; Chi et al., 2014; Li et al., 2015, 2016a). A primary ion beam of Cs^+ with kinetic energy of 12 keV and a current of 1.2–1.5 nA was focused to a 30 × 30–50 × 50 square micron spot for 240 s. To avoid surface contamination, ions were collected from the central 15 × 15–30 × 30 square micron area. Calibration for carbon and water were performed by obtaining $^{12}C/^{30}Si$ and $^{1}H^{16}O/^{30}Si$ intensity ratios in standard basaltic glasses, which was determined by FTIR measurement or manometry (Helo et al., 2011). For each spot, 6–10 cycles of ion intensities were measured. If the ion intensities did not remain stable through the cycles, owing likely to contamination, the selected spot analysis was treated as contaminated and rejected. SIMS analyses were performed for glassy silicate melts quenched from 6 GPa experiments only because it has been demonstrated previously that the obtained intensity ratios tend to be variable, if collected from the melt domains that comprise quenched mineral aggregates (Dasgupta et al., 2013; Chi et al., 2014).

3. RESULTS

Representative textures and phase assemblages of our experiments are shown in Fig. 3 and a summary of experimental conditions, phase assemblages, and key solubility and partitioning data are tabulated in Table 2. Detailed major element and volatile compositions of the resulting phases are reported in Tables 3 and 4.

3.1. Phase assemblage and Texture

All experiments include quenched Fe-Ni-S alloy liquid blobs embedded in silicate melts. Experiments at 6 GPa in graphite capsules produced glassy silicate melt pools for 9 out of 18 samples (Fig. 3a and b). Experiments at 10–13 GPa using MgO capsules produced dendritic crystal aggregates in silicate melt (Fig. 3c–f). Silicate melts were

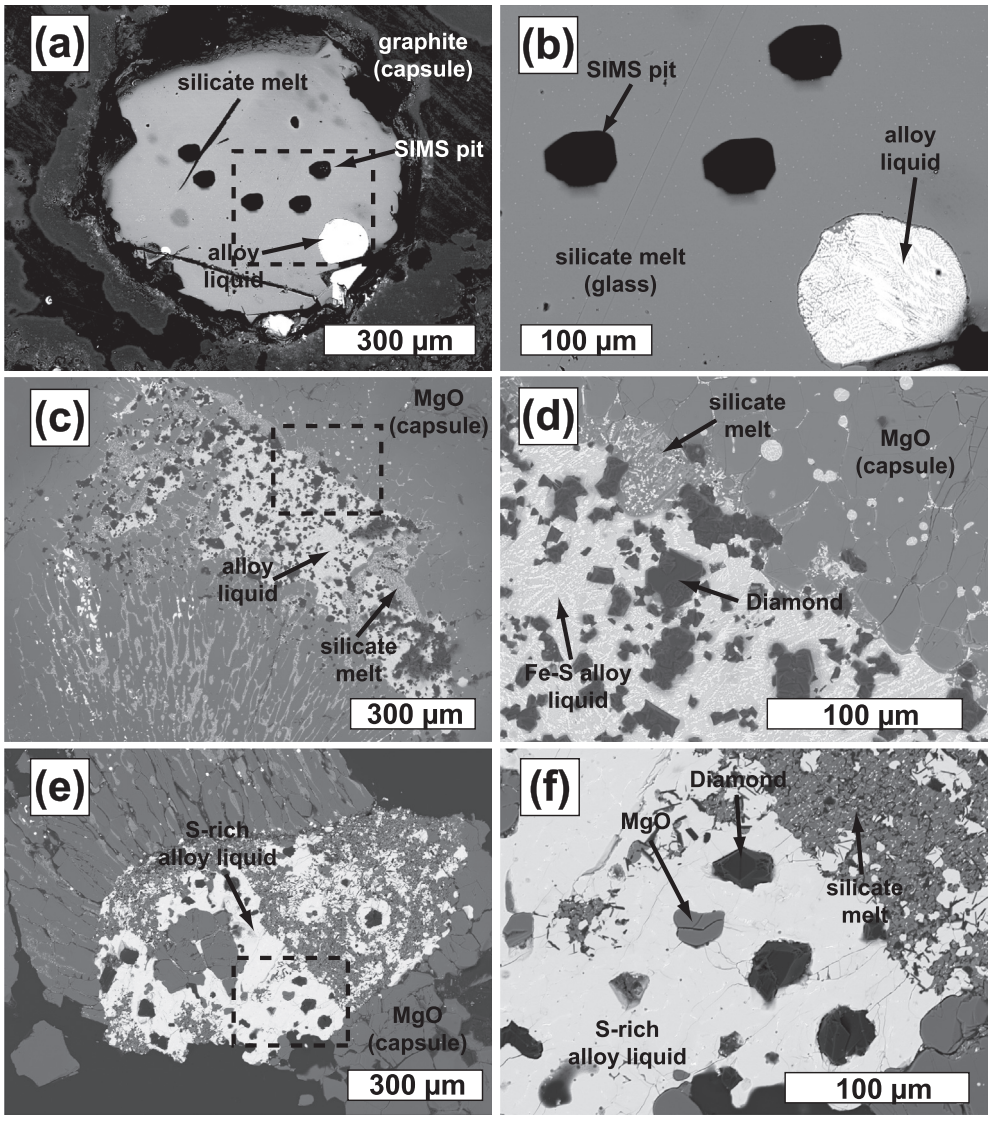

Fig. 3. Representative back-scattered electron images of the experimental run products. (a) Experiment at 6 GPa and 1800 °C (MA144-10S) showing a longitudinal section of alloy – silicate run charge in graphite capsule. (b) A magnified image of panel (a). The run charge includes S-poor alloy liquid which consists of large Fe-Ni quench crystals embedded in grey, small matrix of sulfide-rich alloy. The light grey, homogeneous phase is silicate glass with submicron size of quenched sulfide blob. (c and e) Experiments at 10 GPa and 1800 °C (panel c for MA173-20S and panel e for MA 173-36S) showing longitudinal sections of alloy – silicate run charge in MgO capsule. In both run charges silicate melt percolated into MgO capsule but did not come in contact with the silicate melt from other sample chambers (see Fig. 1b). (d and f) Show details of the quenched liquid from panel (c) and (e), respectively. Alloy liquids were composed of (d) small Fe-Ni quench crystals embedded in large matrix of sulfide alloy and (e) quenched sulfide granular crystals. Both alloys are in contact with diamond, indicating that obtained C concentrations in the alloys are carbon saturated.

observed to percolate partially into the MgO capsules (Fig. 3c and e), but they did not come in contact with the rhenium heaters (Fig. 2b). The recovered products of alloy liquids with ~ 20 wt% S were composed of Fe-Ni dendrites with sulfide matrix (Fig. 3b and d), and those with 36 wt% S were quenched sulfide granular crystals (Fig. 3f).

3.2. Major element compositions in the silicate melt and sulfur-rich alloy liquid and estimation of oxygen fugacity

Major element compositions of alloy and silicate melts are shown in Tables 3 and 4, respectively. For all *P-T* conditions, concentrations of Fe, Ni, S and O in the alloy didn't significantly change for a given bulk composition. FeO content in the silicate melt of four recovered products was higher (~20–23 wt%) compared with the starting BCR-2 composition (~12.5 wt%) due to potential oxidation of the starting alloy mixes.

The oxygen fugacity, fO_2 can be described through equilibrium

$$FeO^{\text{silicate melt}} = Fe^{\text{alloy liquid}} + 0.5O_2 \quad (1)$$

from which fO_2 relative to the iron–wüstite buffer (ΔIW) is defined by

Table 3
Major element compositions (in wt.%) of alloy liquid at 6–13 GPa.

Run. No	P (GPa)	T (°C)	*n*	Fe	Ni	C	S	O	Total
MA145-10S	6	1800	25	85.1(7)	–	4.3(2)	9.4(5)	0.60(17)	99.4
MA145-20S	6	1800	22	75.2(7)	–	1.8(2)	21.2(7)	0.86(26)	99.0
MA145-36S	6	1800	26	62.1(3)	–	0.36(10)	34.7(3)	1.5(2)	98.7
MA142-10S	6	1800	18	79.7(2)	5.0(8)	4.0(6)	10.3(10)	0.21(9)	99.3
MA142-20S	6	1800	15	69.9(5)	5.1(2)	1.4(2)	22.5(5)	0.49(17)	99.3
MA142-36S	6	1800	21	57.2(2)	3.9(4)	0.27(13)	36.0(2)	1.4(1)	98.8
MA144-10S	6	1800	24	70.8(1)	14.3(7)	3.4(2)	11.4(13)	0.17(9)	100.0
MA144-20S	6	1800	12	58.8(1)	16.3(2)	0.83(19)	22.3(33)	1.0(4)	99.3
MA144-36S	6	1800	19	47.0(3)	15.8(1)	0.21(16)	34.8(2)	1.0(1)	98.9
MA158-10S	6	2000	25	85.7(2)	–	4.6(8)	9.5(10)	0.30(2)	100.0
MA158-20S	6	2000	21	74.1(2)	–	1.7(2)	23.2(18)	0.57(12)	99.5
MA158-36S	6	2000	11	63.8(9)	–	0.26(8)	33.0(13)	1.6(5)	98.6
MA152-10S	6	2000	23	81.8(4)	4.8(2)	4.5(2)	10.2(4)	0.18(4)	101.5
MA152-20S	6	2000	15	71.9(6)	4.5(2)	1.5(2)	22.7(11)	0.27(8)	100.9
MA152-36S	6	2000	17	55.7(4)	4.8(7)	0.59(36)	36.9(3)	1.1(2)	99.1
MA160-10S	6	2000	15	67.4(5)	15.3(6)	3.2(1)	13.4(7)	0.28(8)	99.6
MA160-20S	6	2000	18	55.2(2)	16.8(3)	1.2(2)	24.3(1)	0.82(34)	98.3
MA160-36S	6	2000	22	44.9(5)	16.0(2)	0.61(15)	36.3(2)	1.2(1)	99.0
MA173-10S	10	1800	18	84.1(8)	–	4.13(3)	10.1(4)	0.25(8)	98.5
MA173-20S	10	1800	10	76.3(4)	–	1.8(1)	20.9(11)	0.55(33)	99.6
MA173-36S	10	1800	16	62.4(7)	–	0.18(2)	35.8(12)	0.55(8)	99.0
MA168-10S	10	1800	18	77.0(8)	6.2(3)	3.5(2)	12.2(6)	0.14(13)	99.1
MA168-20S	10	1800	15	69.9(6)	4.9(5)	1.4(2)	22.5(8)	0.78(39)	99.5
MA168-36S	10	1800	22	56.4(4)	4.6(1)	0.15(8)	36.8(1)	0.54(8)	98.5
MA169-10S	10	1800	16	66.3(6)	16.9(7)	3.9(2)	11.9(5)	0.37(9)	99.3
MA169-20S	10	1800	14	59.3(6)	15.6(4)	1.6(3)	21.6(9)	0.54(8)	98.6
MA169-36S	10	1800	17	46.5(3)	16.8(7)	0.25(9)	34.9(4)	0.51(14)	98.9
MA174-10S	13	1800	11	69.3(3)	15.2(6)	3.9(1)	11.0(2)	0.33(9)	99.8
MA174-20S	13	1800	18	58.3(5)	17.5(2)	1.6(7)	22.3(1)	0.20(3)	99.9
MA174-36S	13	1800	18	49.3(5)	15.3(2)	0.16(6)	34.2(2)	0.59(6)	99.6

Si was not detected in any of the experimental alloys.
All errors, reported in parentheses, are 1-σ based on replicate EPMA analyses and are reported as the last digit cited. 85.1(7) should be read as 85.1 ± 0.7 wt%.
n is the number of measurements to obtain the compositions reported.

$$\Delta IW = 2 \times \log\left(\frac{a_{FeO}^{\text{silicate melt}}}{a_{Fe}^{\text{alloy liquid}}}\right) = 2 \times \left(\frac{\gamma_{FeO}^{\text{silicate melt}} X_{FeO}^{\text{silicate melt}}}{\gamma_{Fe}^{\text{alloy liquid}} X_{Fe}^{\text{alloy liquid}}}\right) \quad (2)$$

where $a_{FeO}^{\text{silicate melt}}$, $\gamma_{FeO}^{\text{silicate melt}}$, and $X_{FeO}^{\text{silicate melt}}$ are activity, activity coefficient, and mole fraction of FeO in silicate melt, respectively. The fO_2 calculations using the non-ideal solution model were performed assuming that $\gamma_{FeO}^{\text{silicate melt}}$is 1.5 (Holzheid et al., 1997; O'Neill and Eggins, 2002). $\gamma_{Fe}^{\text{alloy liquid}}$ was calculated using ε approach in Wagner equations which incorporates non-ideal interactions amongst the different constituents in the alloy melt (Ma, 2001). We calculated activity of Fe in the alloy melt using the 'Online Metal Activity Calculator' (http://www.earth.ox.ac.uk/~expet/metalact) provided by the University of Oxford. The calculated ideal fO_2 values lie in the range of IW −1.67 to −0.67 and the calculated non-ideal fO_2 values lie in the range of −2.33 to −0.37.

3.3. Carbon solubility in S-rich alloy liquid and silicate melt and $D_C^{\text{alloy/silicate}}$

Carbon was measured in graphite/diamond saturated S-rich alloy liquid using EPMA for all recovered products (Table 3). We observed that alloy C content decreases with increasing alloy S content at a given Ni content and temperature (Fig. 4a). There is no discernible effect of Ni on the C solubility in the S-rich alloy liquid (Fig. 4a). This observation is in contrast to the previously observed negative effects of Ni on C solubility in Fe-rich, S-free alloy melt (Chi et al., 2014). Additionally, Fig. 4b clearly shows that at the relevant *P* (>2 GPa)–*T* (1800–2000 °C) range, *P* has a secondary effect on C solubility in comparison to S content in the alloy. For example, for starting alloy materials with 15 wt% Ni and at 1800 °C, C content is 3.4 ± 0.2 wt% (6 GPa), 3.9 ± 0.2 wt% (10 GPa) and 3.9 ± 0.1 wt% (13 GPa) for relatively low S contents (~11.0–12 wt%), while for high S contents (~33–36 wt%), C contents are 0.21 ± 0.16 wt% (6 GPa), 0.25 ± 0.09 wt% (10 GPa) and 0.16 ± 0.06 wt% (13 GPa) (Table 3).

C-solubility in silicate melt ranges from 13 to 215 ppm for ΔIW between −1.6 and −0.4 (Table 2). Our experimental data are broadly consistent with the previous results on C solubility in reduced basaltic melts at vapor undersaturated and graphite saturated conditions containing 0–0.3 wt% S (Supplementary Fig. 2) (Dasgupta et al., 2013; Chi et al., 2014; Stanley et al., 2014; Armstrong et al., 2015; Li et al., 2015, 2016a, 2017; Duncan et al.,

Table 4
Major element compositions (in wt.%) of silicate melt at 6 GPa.

Run. No	P (GPa)	T (°C)	*n*	SiO_2	TiO_2	Al_2O_3	FeO*	MnO	MgO	NiO	CaO	Na_2O	K_2O	P_2O_5	S	Total	NBO/T
MA145-10S	6	1800	9	52.8(3)	2.1(1)	13.2(2)	16.1(3)	0.20(3)	3.5(1)	–	6.6(1)	2.8(2)	1.7(0)	0.02(1)	0.08(2)	99.1	0.63
MA145-20S	6	1800	11	53.4(2)	2.0(1)	13.7(2)	15.2(3)	0.20(3)	3.5(1)	–	6.7(2)	2.4(1)	1.7(0)	0.07(2)	0.12(2)	99.0	0.58
MA145-36S	6	1800	12	53.8(3)	2.1(1)	13.2(2)	16.1(3)	0.20(2)	3.5(1)	–	6.6(1)	2.8(2)	1.7(0)	0.01(1)	0.17(2)	100.2	0.62
MA142-10S	6	1800	7	53.1(2)	2.0(1)	13.1(1)	17.0(3)	0.18(5)	3.2(1)	0.03(1)	6.4(1)	3.0(1)	1.8(1)	0.02(1)	0.09(1)	99.8	0.64
MA142-20S	6	1800	10	53.1(2)	2.1(1)	13.2(1)	16.6(5)	0.21(4)	3.5(1)	0.03(2)	6.6(1)	3.1(1)	1.8(1)	0.05(2)	0.11(1)	100.2	0.64
MA142-36S	6	1800	12	53.3(8)	2.0(1)	14.0(4)	14.9(24)	0.16(4)	3.7(3)	0.06(4)	6.9(3)	3.0(3)	1.1(1)	0.24(3)	0.21(5)	99.6	0.59
MA144-10S	6	1800	9	50.6(3)	1.9(0)	13.1(1)	20.0(5)	0.21(1)	3.3(1)	0.05(6)	6.2(1)	2.6(1)	1.6(0)	0.04(1)	0.09(3)	99.7	0.72
MA144-20S	6	1800	9	52.3(2)	1.7(1)	10.3(5)	20.0(3)	0.15(3)	2.9(1)	0.17(9)	6.4(2)	2.7(1)	2.0(3)	0.18(4)	0.15(3)	98.9	0.79
MA144-36S	6	1800	11	52.5(2)	2.0(1)	13.3(1)	13.9(2)	0.17(3)	3.6(1)	0.06(4)	6.6(1)	2.4(1)	1.9(0)	0.28(3)	0.15(4)	96.9	0.57
MA158-10S	6	2000	10	52.7(7)	1.9(1)	13.6(2)	14.6(10)	0.2(2)	3.4(2)	–	6.5(2)	2.8(1)	1.7(0)	0.10(3)	0.15(2)	97.7	0.57
MA158-20S	6	2000	8	55.7(9)	2.1(1)	14.0(1)	9.6(2)	0.19(2)	3.7(0)	–	7.2(2)	3.1(2)	1.9(0)	0.25(3)	0.24(2)	97.9	0.47
MA158-36S	6	2000	11	55.7(6)	2.2(1)	14.0(3)	9.7(2)	0.2(3)	3.6(1)	–	7.2(1)	3.2(2)	1.9(1)	0.30(4)	0.43(5)	98.4	0.47
MA152-10S	6	2000	9	52.0(4)	2.1(1)	13.4(2)	14.2(4)	0.20(3)	3.6(1)	0.01(1)	6.6(1)	2.6(1)	1.7(1)	0.03(3)	0.18(3)	96.7	0.59
MA152-20S	6	2000	10	53.5(3)	2.1(1)	13.4(1)	14.7(4)	0.21(3)	3.6(1)	0.02(2)	6.5(1)	2.6(1)	1.7(1)	0.03(2)	0.23(5)	98.6	0.58
MA152-36S	6	2000	8	53.5(5)	1.9(1)	14.7(3)	15.5(3)	0.11(3)	3.3(1)	0.05(5)	5.5(1)	2.3(1)	1.5(0)	0.15(3)	0.38(3)	98.8	0.51
MA160-10S	6	2000	6	48.7(3)	1.9(1)	11.8(1)	22.6(2)	0.16(2)	3.0(1)	0.09(6)	6.0(1)	2.5(0)	1.5(1)	0.08(4)	0.23(3)	98.5	0.85
MA160-20S	6	2000	6	50.4(4)	1.6(1)	11.9(1)	22.8(4)	0.11(2)	3.0(1)	0.18(3)	6.0(2)	2.2(1)	1.5(2)	0.15(4)	0.37(6)	99.2	0.78
MA160-36S	6	2000	8	54.8(4)	2.0(2)	13.6(1)	12.6(2)	0.18(2)	3.5(1)	0.11(5)	6.5(1)	2.5(1)	1.8(0)	0.28(4)	0.29(4)	98.3	0.51

All errors, reported in parentheses, are 1-σ based on replicate EPMA analyses and are reported as the last digit cited. 52.8(3) should be read as 52.8 ± 0.3 wt%.
n is the number of measurements to obtain the compositions reported.
NBO/T calculations are using average values for the oxides or metals.

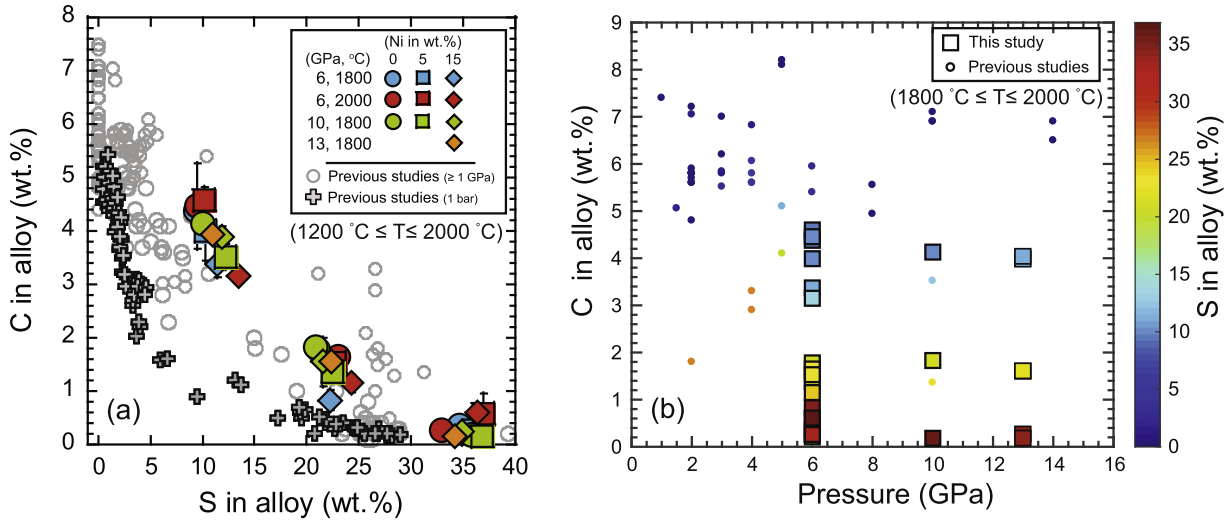

Fig. 4. (a) C solubility (in wt.%) in Fe-Ni-S alloy liquid as a function of S content. Our datasets are grouped to show the effects of pressure, temperature, and alloy Ni content. Also plotted for comparison are C solubility data for Fe-Ni alloy liquids previously reported (see the caption of Fig. 1 for references), (b) C solubility (in wt.%) in the Fe-Ni alloy as a function of pressure and S content in the alloy. Along with the new experimental results from our study also plotted for comparison are previous data ranging from 1800 and 2000 °C.

2017). We calculated $D_C^{alloy/silicate}$ based on the carbon content in the alloy liquid and silicate melt. $D_C^{alloy/silicate}$ ranges from 3493 ± 289 to 53 ± 22, decreasing with increasing S content in alloy liquid. $D_C^{alloy/silicate}$ varies from 703 ± 146 to 3493 ± 289 for 9–11.5 wt% S and from 53 ± 22 to 1254 ± 116 for 20.5–25.5 wt% S in the alloy liquid (Fig. 5), with lower $D_C^{alloy/silicate}$ at higher T.

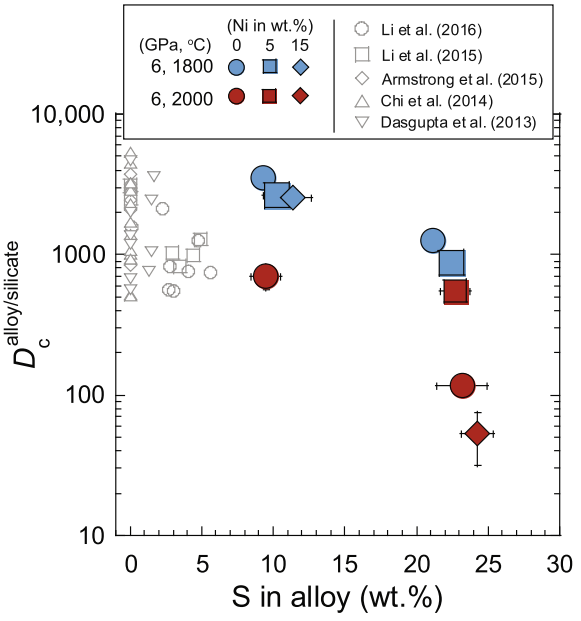

Fig. 5. $D_C^{alloy/silicate}$ as a function of S content in the alloy liquid. Also plotted for comparison are data from previous studies (Dasgupta et al., 2013; Chi et al., 2014; Armstrong et al., 2015; Li et al., 2015, 2016a). The data from this study are grouped according to pressure, temperature, and Ni content of the alloy liquids.

3.4. Sulfur content in basaltic silicate melt

Sulfur content in silicate melts shows a positive dependence on bulk S content and temperature. S content in silicate melt increases from 0.08 ± 0.02 to 0.21 ± 0.05 wt% with increasing S content in alloy liquids from 9.4 to 36.0 wt% at 1800 °C and from $\sim 0.15 \pm 0.03$ to $\sim 0.43 \pm 0.05$ wt% with increasing S content in alloy liquids from 9.5 to 33.0 wt% at 2000 °C (Table 4). The positive dependence of S content in silicate melt on T and near T independence of S content in alloy liquid means that with increasing S content in the alloy liquid, $D_S^{alloy/silicate}$ varies between 111 ± 21 to 199 ± 24 at 1800 °C and from 54 ± 6 to 127 ± 18 at 2000 °C (Supplementary fig. 3).

4. DISCUSSION

4.1. The effects of sulfur, nickel, pressure, and temperature on carbon solubility in alloy liquids

A key observation of our new experimental data is a decrease of C solubility with increase in S content of Fe-alloy liquids containing relevant range of Ni content and P-T appropriate for alloy-silicate partitioning in magma oceans of terrestrial bodies (Fig. 4). A similar effect in high P-T experiments has been previously reported based on C solubility in both Ni-rich sulfide alloy liquids (Tsuno and Dasgupta, 2015; Zhang et al., 2018) as well as Ni-free, S-bearing alloys (Dasgupta et al., 2009; Deng et al., 2013). Using our experimental results along with previously published solubility data of C in Fe-Ni-S alloys from ambient pressure to high-pressures, we parametrized C solubility in alloy liquids as a function of pressure and temperature as well as Ni and S contents in the alloy liquid:

$$\begin{aligned}\ln C\ (\mathrm{wt.\%}) &= -33.59(\pm 2.22) - 2726(\pm 579)/T \\ &\quad - 38.7(\pm 28.9) \times (P/T) \\ &\quad + 7.51(\pm 0.40) \times \ln(100 - X_S) \\ &\quad + 0.48(\pm 0.21) \times \ln(100 - X_{Ni}) \end{aligned} \quad (3)$$

where T is temperature in K, P is pressure in GPa, and $X_{\mathrm{s\ and}}$ X_{Ni} are mass fraction of S and Ni (in wt.%), respectively. Fig. 6 shows how well Eq. (3) can capture the variability of the experimentally measured Ln(C, wt.%) in Fe-rich alloy liquid. We note that the experimental data obtained under reduced conditions ($\Delta IW \leq -2.5$) were not included for parameterization because the presence of Si which is dissolved in alloy under reduced conditions would significantly affect the C solubility in the alloy (Li et al., 2015, Li et al., 2016a). Our regression result indicates a significant increase of C solubility with increasing temperature, whereas pressure has a minor effect on C solubility. We also observed a strong decrease of C solubility with increasing S content in the alloy and a slight decrease with increasing Ni content in the alloy. The effect of Ni in reducing C solubility in Fe-rich alloy diminishes with increasing S content of the alloy, similar to the observation of Zhang et al. (2018). However, in contrast to the empirical parameterization of Zhang et al. (2018), which does not include any effect of P and T on C solubility, our parameterization combines the effects of alloy composition (Ni and S content) as well as those of P and T.

4.2. Comparison with previous studies on C partitioning between S-poor alloy liquid and silicate melt

The new dataset provides the first constraints on C partitioning between S- and Fe-rich alloy liquid and mafic silicate melt at graphite saturation, as previous studies have exclusively focused on C partitioning in S-poor systems (Dasgupta et al., 2013; Armstrong et al., 2015; Li et al., 2016a; Duncan et al., 2017; Chi et al., 2014). Because the experimental silicate melt compositions (e.g., FeO content and NBO/T), pressure, and temperature vary between our study and previous studies, to chiefly constrain the effect of S on C partitioning, the data in this study was compared against the empirical relationships formulated in previous studies (Chi et al., 2014; Li et al., 2016a, 2015; Duncan et al., 2017; Li et al., 2017) at a fixed pressure, temperature, silicate melt composition, and oxygen fugacity relevant to our study. Using parameterizations from previous studies, carbon partitioning between S-free alloy liquids and silicate melt was calculated at our experimental P-T condition (6 GPa-1800 °C in Fig. 7a and 6 GPa-2000 °C in Fig. 7b) and silicate melt compositions (NBO/T in the range of 0.5–0.8, see Table 2). Fig. 7 shows that $D_C^{\mathrm{alloy/silicate}}$ for $\Delta IW < -1$ and at 1800 °C and $D_C^{\mathrm{alloy/silicate}}$ at 2000 °C is lower than the relationship for S-free alloys because of the lower C solubility for S-rich alloy compared with the one for S-free alloy. A similar observation can be made also in Fig. 5, where it can be noted that for alloy S content ~22–24 wt%, $D_C^{\mathrm{alloy/silicate}}$ values for 2000 °C experiments are distinctly lower compared to those in systems with Fe-rich alloy containing <20 wt% S. $D_C^{\mathrm{alloy/silicate}}$ for 2000 °C is lower compared with that for 1800 °C owing to the higher C solubility in silicate melt at 2000 °C (Tables 2 and 4). $D_C^{\mathrm{alloy/silicate}}$ for $\Delta IW > -1$ and at 1800 °C is comparable to the relationship for S-free alloy because C solubility in the alloy liquid with 9–12 wt% S is lower than S-free alloy whereas C solubility in the silicate melt at 1800 °C in this study is also lower than in the studies of Li et al. (2015, 2016a) and Chi et al. (2014) (Supplementary Fig. 2). We note that the relatively low $D_C^{\mathrm{alloy/silicate}}$ values determined here for a couple of our bulk compositions at 2000 °C and alloy melt containing ~22–23 wt% S are in part due to exclusion of C from S-rich alloy liquid but primarily owing to enhancement of C solubility in silicate melt at graphite saturation with increasing S content of silicate melt (Supplementary Fig. 2). However, it is unclear at present what dissolution mechanism could cause such a strong covariation of C and S in silicate melt at otherwise similar fO_2, P, T conditions. The two low $D_C^{\mathrm{alloy/silicate}}$ values from Figs. 5 and 7b therefore have not been used in any subsequent modeling in this study (see Figs. 8 and 10).

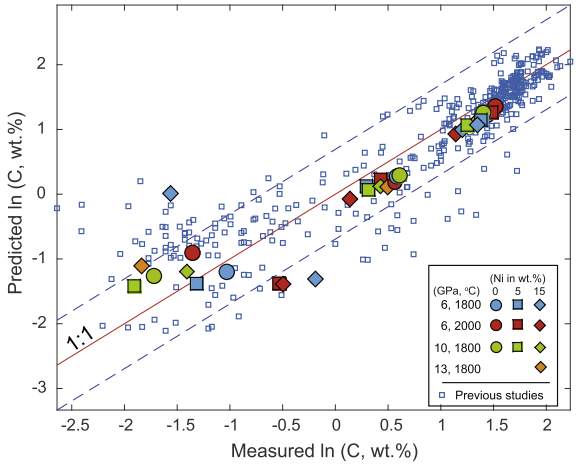

Fig. 6. Comparisons of experimentally determined and predicted C solubility in alloy liquid. Solid line is the 1:1 line, and the dashed lines are 1:2 and 2:1 lines. The symbols showing our experimental results are the same as the ones in Fig. 4a. The data from previous studies includes experiments at ambient as well as high pressure (Wang et al., 1991; Tsymbulov et al., 2001; Dasgupta et al., 2009; Dasgupta et al., 2013; Deng et al., 2013; Chi et al., 2014; Boujibar et al., 2014; Armstrong et al. 2015; Li et al., 2016a, 2015; Zhang et al., 2018).

Although constraining the effect of melt composition on $D_C^{\mathrm{alloy/silicate}}$ for S-rich alloy-silicate system is not a main purpose of this study, here we note that $D_C^{\mathrm{alloy/silicate}}$ for peridotitic (~40 wt% MgO) silicate melt composition, which is more relevant for silicate magma ocean is lower compared with that for systems with basaltic silicate melt (Duncan et al., 2017).

4.3. Origin and initial distribution of carbon in terrestrial planets

Alloy-silicate partitioning values of moderately siderophile elements like Ni and Co have been used to constrain

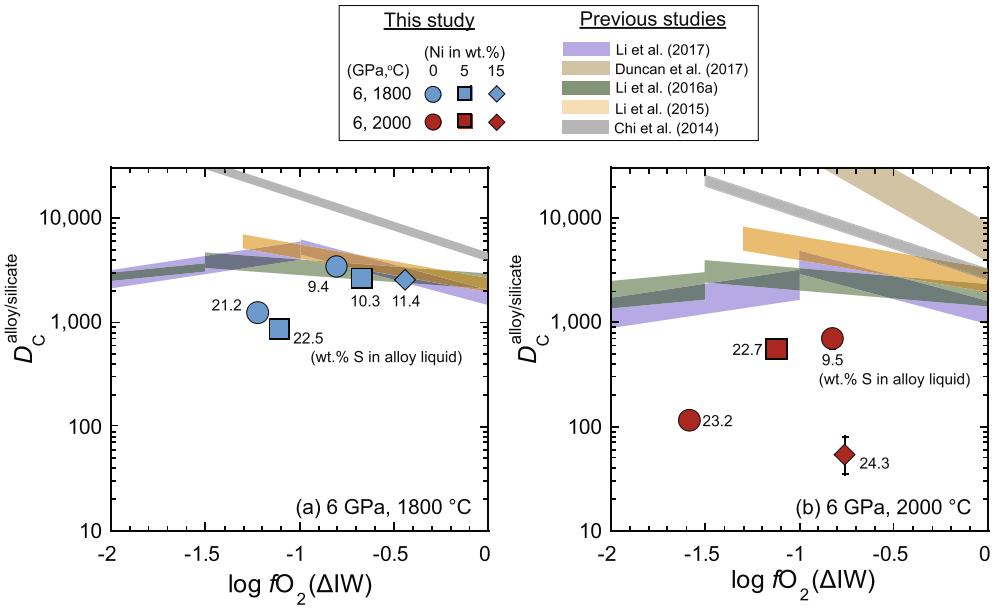

Fig. 7. Variation of $D_C^{alloy/silicate}$ at (a) 6 GPa and 1800 °C and (b) 6 GPa and 2000 °C. Our experimental data are marked by the symbols in blue (a) and in red (b), which are also used in Figs. 4a and 5. The curves for comparison are C partitioning between S-free alloy liquid and silicate melt based on the empirical parameterizations of Li et al. (2017, 2016a, 2015), Duncan et al. (2017), and Chi et al. (2014) with the pressure and temperature conditions same as the data in the two panels. The band widths indicate the variation of NBO/T (between 0.5 and 0.8), which is relevant for our experimental silicate melt (Table 4). The figure shows that in the presence of significant concentration of sulfur in the system, the equilibrium $D_C^{alloy/silicate}$ values are distinctly lower than the previous experimental data and models developed for S-free or S-poor conditions. (For interpretation of the references to colour in this figure legend, the reader is referred to the web version of this article.)

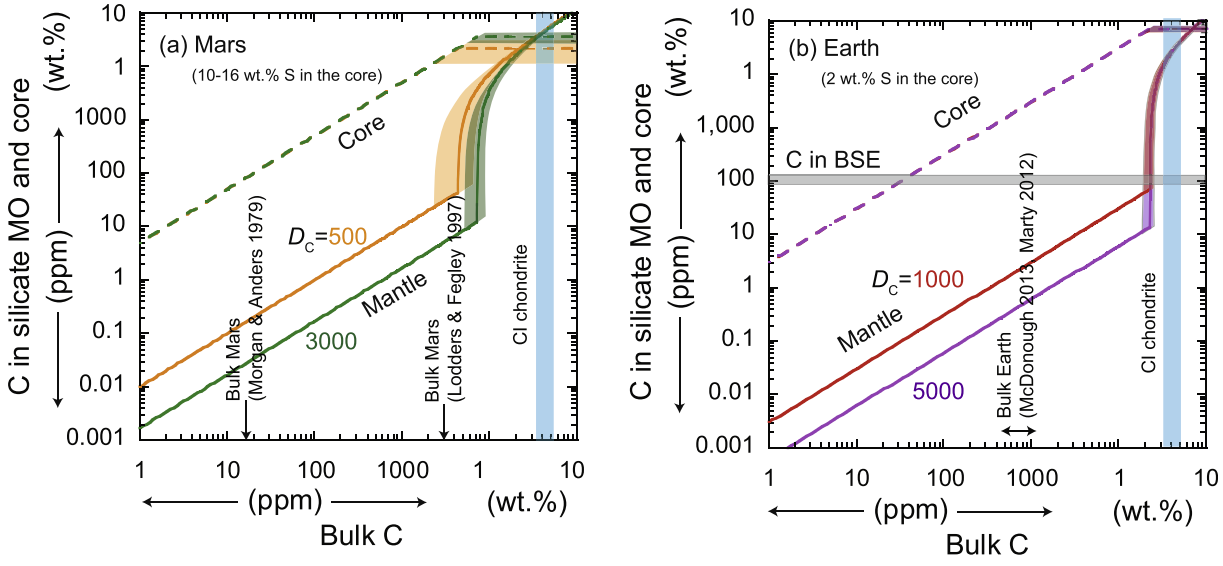

Fig. 8. The predicted carbon content of the mantle (solid lines) and core (broken lines) for Mars (a) and Earth (b), as a function of bulk carbon content. C content in the core and mantle are calculated based on equilibrium C partitioning between S-rich alloy liquid and silicate melt based on our experimental data at 6 GPa and 2000 °C, which is relevant for magma ocean conditions of Mars (Rai and Van Westrenen, 2013) and shallow magma ocean condition of the Earth. For calculating Martian mantle and core composition, core: bulk Mars mass ratio = 0.20 (Urakawa et al., 2004; Wang et al., 2013), $D_C^{alloy/silicate}$=500–3000, and C_C^{alloy} (C solubility in the alloy liquid) = 3.5(±0.9) – 2.3(±0.9) wt.% for the alloy core with 10–16 wt% S are used. For calculating Earth's mantle and core carbon contents, core: bulk Earth mass ratio = 0.33, $D_C^{alloy/silicate}$= 1000–5000, and C_C^{alloy} = 5.8 (±0.9) wt.% are used. The purpose of this figure is to showcase the effect of sulfur alone on the equilibrium fractionation difference of carbon between Earth and Mars. In reality the applicable $D_C^{alloy/silicate}$ value for terrestrial MO fractionation is expected to be higher owing to strong positive effect of pressure on $D_C^{alloy/silicate}$ and the expectation that the base of the MO for Earth likely was quite deep (e.g., Chi et al., 2014; Li et al., 2015).

P–T conditions of MO equilibration and the redox state of the planetary accretion (e.g., Kegler et al., 2008; Bouhifd and Jephcoat, 2011; Siebert et al., 2013; Badro et al., 2015; Fischer et al., 2015). For Mars, the siderophile element partitioning data favors an averaged single-stage equilibration at the base of an MO at pressures of 10–17 GPa and oxygen fugacity of $\Delta IW \sim -2$ to -1 (Righter and Chabot, 2011; Rai and Van Westrenen, 2013). On the other hand, proposed accretion processes for Earth vary from an averaged single-stage core formation at a fixed P–T–fO_2 condition (Corgne et al., 2009; Righter, 2011; Walter and Cottrell, 2013) to multi-stage accretion process with evolving composition and redox state of the building blocks (Wade and Wood, 2005; Rubie et al., 2011; Tuff et al., 2011; Wade et al., 2012; Rubie et al., 2015; Badro et al., 2015). Some continuous accretion models prefer increasing oxygen fugacity during accretion and a gradual increase in FeO content of bulk silicate Earth (O'Neill, 1991; Rubie et al., 2011; Tuff et al., 2011; Wade et al., 2012; Rubie et al., 2015; Clesi et al., 2016) whereas few recent models suggest a decrease in the fO_2 of the terrestrial MO with progressive accretion (Siebert et al., 2013; Badro et al., 2015; Wade and Wood, 2016). However, none of these homogeneous and continuous accretion models can explain the required volatile budget, especially C and S abundances in BSE (e.g., Li et al., 2016a).

The chemical compositions of the building blocks of the terrestrial planets are proposed based on the isotope data as well as the abundances of trace elements and volatiles such as C and S. For Earth, both reduced, enstatite-chondrite type material (e.g., Javoy et al., 2010; Dauphas, 2017) as well as oxidized, volatile-rich, carbonaceous-chondrite type material (Palme and O'Neill, 2013; Sarafian et al., 2014) have been proposed as the building blocks. Li et al. (2016a) argued that the late stage accretion of differentiated planetary embryos (~10–20 wt% of total present-day Earth mass; O'Neill, 1991; Boujibar et al., 2014; Wade and Wood, 2016; Wohlers and Wood, 2015; 2017) with either S-rich or Si-rich cores to a volatile-free proto-Earth satisfies the present day C/S ratio in BSE.

Here we discuss the initial inventory of carbon and sulfur in Earth and Mars based on our new experimental and parameterization results in conjunction with geochemically proposed C and S concentrations to show that homogeneous and equilibrium core formation results in vastly different C budget in the silicate portion of Earth and Mars for a given concentration of carbon available during core formation. To evaluate potential similarity or dissimilarity in the carbon budget of bulk silicate Earth and Mars, we also consider that Mars is a planetary embryo that lacked continued phase of accretion with late addition of large differentiated bodies whereas the Earth grew larger through late giant impacts. For the latter, we employ our experimental dataset in the model framework of Li et al. (2016a), which allowed complete MO equilibration to take place during the differentiation of the impactor itself but called for a direct merger of the mantle of the impactor with the mantle of the proto-Earth without any equilibration of the impactor's core with proto-Earth' mantle. C and S fractionation in the MO of the planetary embryo in the model of Li et al. (2016a) was based on the datasets of C solubility and partitioning involving an S-poor alloy liquid ($\leq$~5 wt% S) up to 8 GPa and previously published C solubility in S-rich (~36 wt%) alloy liquids at ambient pressure. Using our new experimental and parametrization results on C solubility in S-rich alloy liquid and C partitioning between S-rich alloy liquid and silicate melt for the relevant conditions, in the following we determine whether the budgets of volatiles such as C and S in the modern Earth could have been established by the accretion of a C- and S-bearing planetary embryo to a proto-Earth that is virtually volatile-free in its silicate fraction. Although some geochemical models postulate the delivery of volatiles in the early stage of accretion (Marty, 2012; Sarafian et al., 2014), the simulation results indicate that proto-Earth includes volatile-poor (S-type) materials much more than volatile-rich (C-type) material (Walsh et al., 2012; O'Brien et al., 2014). Therefore, the choice of volatile-free proto-Earth may not be an unrealistic approximation to discuss the transport of volatiles during the heterogeneous core-formation process. On the other hand, the modeling presented below does not require the proto-Earth to be volatile free but rather the silicate portion of the proto-Earth to be devoid of C and S. Virtually C-free silicate portion of the proto-Earth is expected given the extremely siderophile nature of C at deep MO condition where the equilibrating alloy is S-poor (e.g., Chi et al., 2014; Li et al., 2015).

4.3.1. Predicted initial distribution of carbon in the Earth and Mars based on homogeneous equilibrium accretion model: The role of sulfur

To test the effect of single stage core-mantle equilibration for initial distribution of carbon in Earth and Mars, we calculated the fractionation of C between the cores and mantles taking into account the constraints for S content in the core (Earth: 2 wt%) (Allègre et al., 1995; Dreibus and Palme, 1996) (Mars: 10–16 wt%) (Lodders and Fegley, 1997; Sanloup et al., 1999; Rai and Van Westrenen, 2013). The mass fraction of Earth's core is fixed at 0.33, while for Mars' core it is fixed at 0.20 (Urakawa et al., 2004; Wang et al., 2013). If the core of Earth and Mars is C-undersaturated, then the distribution of C in the mantle and core ($X_C^{\text{mantle or core}}$) is obtained by the equation;

$$X_C^{\text{mantle}} = \frac{X_C^{o}}{M^{\text{core}} \times D_C^{\text{alloy/silicate}} + (1 - M^{\text{core}})} \quad (4)$$

$$X_C^{\text{core}} = \frac{X_C^{o} - (1 - M^{\text{core}}) \times X_C^{\text{mantle}}}{M^{\text{core}}} \quad (5)$$

where X_C^{o} indicates the bulk C content of the Earth or Mars that participated in alloy-silicate fractionation and M^{core} represents mass fraction of their cores.

However, if the core of Earth or Mars is C-saturated, then C concentration in the mantle is obtained by the equation;

$$X_C^{\text{mantle}} = \frac{X_C^{o} - M^{\text{core}} \times C_C^{\text{alloy}}}{1 - M^{\text{core}}} \quad (6)$$

where C_C^{alloy} ($=X_C^{\text{Core}}$) is concentration of C in the core, which is equivalent to the C solubility limit in the alloy liquid.

For calculating C content in the Martian mantle and core, we employ $D_C^{alloy/silicate}$ for a core with 10–16 wt% S (Lodders and Fegley, 1997; Sanloup et al., 1999; Rai and Van Westrenen, 2013). We note that the estimated S content of the Martian core is distinctly higher than that estimated for the Earth (2 wt%; Allègre et al., 1995; Dreibus and Palme, 1996). Based on the higher S content of the equilibrating alloy, we apply $D_C^{alloy/silicate}$ ranging from 500 to 3000 based on our experimental results (Fig. 5). The carbon content that took part in alloy-silicate fractionation for Mars remains uncertain. However, if we assume that the estimated bulk Mars C content was available throughout the episodes of core formation, then the relevant X_C^o value could be between 16 ppm (Morgan and Anders, 1979) and 2960 ppm (Lodders and Fegley, 1997). This range encompasses bulk Earth carbon content of ~700–1000 ppm (McDonough and Sun, 1995; Marty, 2012). Employing 1000 ppm C as the bulk Mars carbon yields 1–8 ppm C in the bulk silicate Mars and 0.5 wt% C in the bulk core of Mars (Fig. 8a).

For core-mantle C fractionation of Earth we performed similar calculation but considered that the Earth's core alloy is estimated to be relatively sulfur-poor, i.e., ~2 wt%. Hence in calculating C fractionation, we applied an alloy-silicate C partition coefficient, $D_C^{alloy/silicate}$ of 1000–5000 (Chi et al., 2014; Li et al., 2015, 2016a), which extends to higher values than the range applied for S-rich Martian system. However, to compare the effect of sulfur directly, we kept the fO_2 condition of alloy-silicate equilibration similar to that applied for Mars. For a bulk Earth C content of ~1000 ppm, this yields BSE carbon content of 0.5–3.0 ppm and bulk core carbon content of 0.3 wt% (Fig. 8b). We note that this distribution is calculated taking into account the effect of sulfur in the alloy alone. For terrestrial C fractionation, the applicable $D_C^{alloy/silicate}$ value may be even higher if the positive effect of pressure as constrained in the study of Chi et al. (2014) is applied. Unlike in case of Mars, estimates are available for C content of BSE or the bulk mantle (e.g., 80–120 ppm; Dasgupta and Hirschmann, 2010; Hirschmann, 2016). These values are distinctly higher than the value obtained from equilibrium core formation model shown here. Hence a more complex core formation or post-core formation processes likely were responsible for supplying the C budget of BSE as concluded in previous studies (Dasgupta, 2013; Chi et al., 2014; Li et al., 2016a). The finding here, however, is that for a similarly available budget of carbon during alloy-silicate equilibration, Mars and Earth might have had a distinctly different quantity of carbon retained in the silicate fraction, caused entirely by the sulfur content of the equilibrating alloy. Martian mantle would be less depleted in carbon compared to the mantle of Earth.

4.3.2. Initial budget of carbon in the Earth: heterogeneous equilibrium accretion model

Although equilibrium core formation model produces a residual MO that is distinctly lower in its carbon content than the present-day estimates of C in the BSE, different accretion and core formation process may lead to the C budget of post core formation MO to be similar to that of the modern Earth's mantle. For example, C and S budgets of the BSE have been explained recently by disequilibrium merger of a S-rich planetary embryo to a volatile-free proto-Earth (Li et al., 2016a). Here we test the model of Li et al. (2016a) using the new high pressure data of C solubility in S-rich alloy and $D_C^{alloy/silicate}$ values for high pressure S-rich alloy-bearing systems. Similar to the accretion model of Li et al. (2016a), here we assume a perfect merger of a relatively oxidized C- and S-bearing impactor ($\Delta IW = -1.5 \sim -0.5$; comparable to our experimental range) to a proto-Earth whose bulk silicate fraction is devoid of C and S. We also assume that the cores of both the impactor and the proto-Earth had separated after complete equilibration with their respective overlying molten silicate MO before the collision (Fig. 9). The initial distribution of C and S in the core and the mantle of the impactor are determined based on $D_C^{alloy/silicate}$, $D_S^{alloy/silicate}$, and C solubility limit in the alloy liquid at 6 GPa and 2000 °C that diminishes with increasing S content. As the modelled impactor is S-rich, $D_C^{alloy/silicate}$ is varied between 500 and 1000 based on the range of our experimental data, while given the fact that the experimental $D_S^{alloy/silicate}$ values remain in a narrow range (50–120 at 2000 °C), we used a mean value of 100 for our model calculations. For $D_S^{alloy/silicate}$ lying in a range of 50–120, sulfur content of the core of the impactor is 18–19 wt%, which affects the distribution of C in the mantle and core of the impactor a little. We assumed the mass fraction of the core of the impactor and initial S content of the impactor to be 0.15 (similar to mass fraction of the core in Mars; Urakawa et al. 2004; Wang et al. 2013) and 3.0 wt% (less than S content of CI chondrite; Lodders and Fegley,

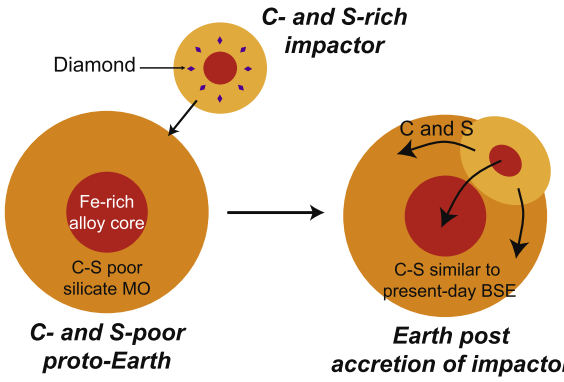

Fig. 9. A schematic diagram illustrating the merger of a C- and S- bearing impacting body to a volatile-free proto-Earth or a proto-Earth whose silicate fraction is C and S-free assuming a simple two-stage core formation. We assume that equilibration was achieved in magma oceans of both the impactor and proto-Earth. We also postulated that the mantle and core of the impactor were directly merged with the mantle and core of the proto-Earth, respectively with minimal interaction between metals and silicates post impact. This cartoon shows that the silicate MO of the impactor would be carbon-rich (graphite or diamond being expelled from the core) owing to the carbon saturation in the S-rich alloy liquid.

1997), respectively. The distribution of S in the impactor's mantle and core is calculated by;

$$X_S^{mantle} = \frac{X_S^o}{M^{core} \times D_S^{alloy/silicate} + (1 - M^{core})} \quad (7)$$

$$X_S^{core} = \frac{X_S^o - (1 - M^{core}) \times X_S^{mantle}}{M^{core}} \quad (8)$$

where X_S^o and M^{core} indicate the bulk S content of the impactor and core mass with respect to the bulk impactor. Using Eqs. (7) and (8) and $D_S^{alloy/silicate}$ of 100, S content in the impactor's mantle and core is calculated to be 1900 ppm and 19 wt%, respectively, and C solubility limit in the alloy liquid containing 19 wt% S is 1.6 ± 0.9 wt%. We varied the C content in the bulk impactor from 0 to 2 wt%, keeping the upper limit to be less than the C content of CI chondrites (Wasson and Kallemeyn, 1998; Pearson et al., 2006). C content in the mantle and core of the impactor can be obtained following Eqs. (4) and (5) when the impactor's core is C-undersaturated, and if the impactor's core is C-saturated, C concentration in the mantle is obtained by Eq. (6), which indicates that the excess carbon which was not dissolved in S-bearing alloy liquid was expelled as graphite or diamond to silicate MO of the impactor (Fig. 9). We used $D_C^{alloy/silicate}$ and $C_C^{alloy}(=X_C^{Core})$ to be 500–1000 and 1.6 ± 0.9 wt%, respectively, for the alloy liquid with 19 wt% S. We varied the impactor: present-day Earth mass ratio between 0.05 and 0.25, which covers a range from the mass of Mercury to about twice the mass of Mars. Further the mantle and core of the impactor are assumed to have perfectly merged with the mantle and core of the proto-Earth, respectively, without any equilibration. This is supported by Deguen et al. (2014) showing the low equilibrium efficiency ($\leqq$0.01) of siderophile elements ($D_i^{alloy/silicate} \geqq \sim 30$, i = Ni and Co) between the core of Mars-sized impactor and the magma ocean of accreting Earth.

The successful scenario for constraining the initial concentration of carbon in the impactor, the mass fraction of the impactor's core, and bulk impactor to Earth mass ratio has to satisfy the C and S contents and C/S ratio in BSE (80–120 ppm, 200–250 ppm, and 0.35–0.63, respectively; Hirschmann, 2016) after the merger of the impactor and the proto-Earth. In Fig. 10a and b, we show an example model which satisfies the geochemical estimates. For the impactor: present-day Earth mass ratio of 0.15, our model calculations show that a differentiated impactor with 1500–4500 ppm bulk C is required to match the BSE C and S abundance.

For full set of calculations with the impactor mass varying between 5 and 25% of the Earth mass and the core mass fraction of the impactor being fixed at 0.15, an impactor

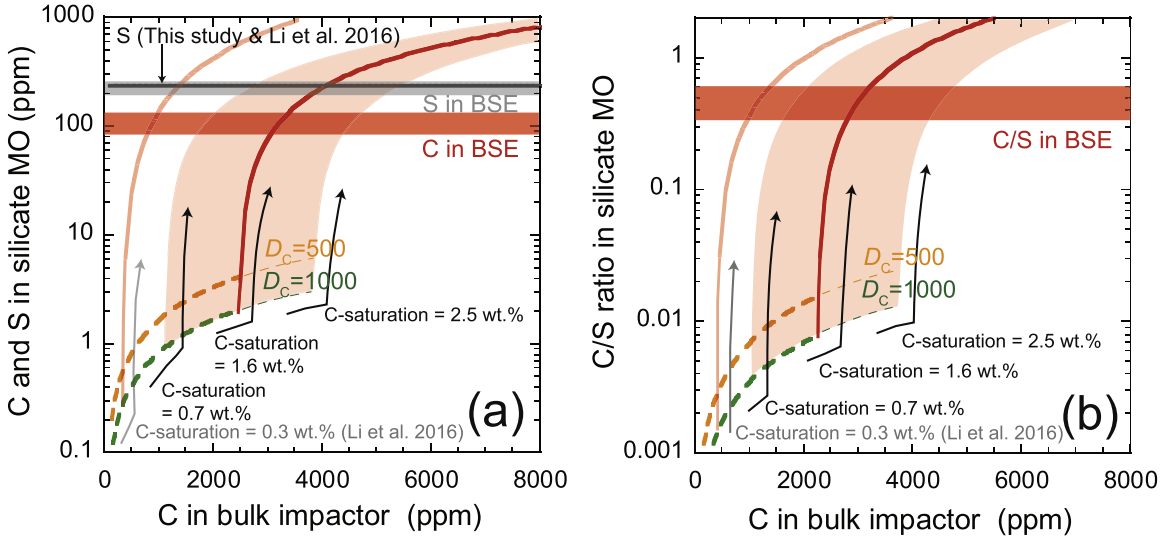

Fig. 10. An example of the models where carbon and sulfur content (a) and C/S ratio (b) in terrestrial post-core formation magma ocean are set by the merger of C- and S-bearing impactor to a proto-Earth with C and S-free mantle. Carbon and sulfur contents and C/S ratio in terrestrial magma ocean after the proto Earth's accretion of the differentiated planetary embryo are plotted as a function of initial C content of the impactor for an impactor:present-day Earth mass ratio of 0.15. We assumed that bulk S content in the impactor and impactor's core mass fraction are 3.0 wt% and 0.15, respectively (see text for more details). For calculating the distribution of C and S in the mantle and core of the impactor, we employed $D_S^{alloy/silicate} = 100$ to obtain the S content of the impactor's core (19 wt%), and $D_C^{alloy/silicate} = 500$–1000 and C_C^{core} or the solubility limit of C to be 1.6 (±0.9) wt.% for the alloy with 19 wt% S. The colored broken curves (in orange and green) indicate C content and C/S ratio in the Earth after the merger with the impactor where the C content in the S-rich impactor's core does not exceed C solubility limit in the alloy liquid with 19 wt% S. The solid curves and area in red denote C content and C/S ratio in post-accretion Earth where C-rich impactor collides with the proto-Earth, i.e., scenarios where C saturation is achieved in the impactor's core (see Fig. 9) considering the regression error of C solubility to be 0.9 wt%. The solid curve in black shows S content in BSE after the accretion. The grey regions and deep red regions denote the C and S contents and C/S ratio of BSE (Hirschmann, 2016; Li et al., 2016a). We also show plots that compare the model calculations presented here with those of the model of Li et al. (2016a) where the solubility limit of C in S-rich impacting core is assumed to be 0.3 wt%. (For interpretation of the references to colour in this figure legend, the reader is referred to the web version of this article.)

that is 9–20% of the mass of Earth can explain the C and S contents and C/S ratio in BSE. The bulk C of the impactor necessary to account for C and S contents and C/S ratio in BSE decreases from ~4750 ppm to ~1700 ppm with increase in the impactor's mass. The required C content in the building blocks of the impactor is distinctly lower than the volatile contents in carbonaceous chondrite (5.0 wt% C in Cl chondrite; Wasson and Kallemeyn, 1998; Pearson et al., 2006), which could be a result of the volatility-induced loss of C and S during accretion processes. Bulk C content of the impactor necessary to explain carbon in BSE constrained in this study is somewhat higher than that in the previous study (~0.13 wt%; Li et al., 2016a and Fig. 10) because C-solubility in S-rich alloy liquid at high pressure parameterized based on our experimental data and published data (Eq. (3)) is higher than the value of ~0.3 wt% used in Li et al. (2016a). Our calculations result in C and S contents in the Earth' core after the merger of the impactor to be ~130–700 ppm and 0.6 wt%, respectively. However, we note that these obtained numbers rely entirely on the model assumption that the proto-Earth was C and S free. If ~2 wt% S in the core based on previous geochemical arguments (Allègre et al., 1995; Dreibus and Palme, 1996) are appropriate, then the giant impactor alone is not able to bring enough S into the core, implying that S-bearing proto-Earth should be considered. However, constraints based on the comparison of the density of the alloy liquid obtained by ab-initio calculation and the density of the core determined by seismic observation accepts a wide range of S content (0–2.4 wt%) (Badro et al., 2014), which is consistent with our estimation. Carbon content in the core obtained here is even lower than the results suggested by previous mineral physics and geochemical mass balance arguments (0.2–1.2 wt% C) (Wood, 1993; Dasgupta and Walker, 2008; McDonough, 2013; Palme and O'Neill, 2013; Wood et al., 2013; Dasgupta, 2013; Chen et al., 2014; Chi et al., 2014; Nakajima et al., 2015; Prescher et al., 2015). However, once again, ~0.07 wt% C in the core suggested here is contributed only from the giant impactor that establishes the C budget of BSE and does not include any C that the core of the proto-Earth might have had. Finally, if the impactor is <9% and >20% of the mass of the Earth to merge into the volatile-depleted proto-Earth, the C content and C/S ratio in BSE would not be simultaneously satisfied for a given bulk impactor C content.

5. CONCLUSIONS

We experimentally constrain that the addition of sulfur decreases the solubility limit of carbon in the Fe-Ni alloy liquid at high pressures and temperatures relevant for segregating alloy liquid at magma oceans of terrestrial planets. Regression derived from our experimental data (6–13 GPa, 1800–2000 °C, and 0–15 wt% Ni in the alloy) and previous data indicates that C solubility significantly increases with increasing temperature whereas the effect of pressure on C solubility is negligible. We also found that C solubility in the alloy liquid strongly decreases with increasing S content and unlike in S-free or S-poor alloy where Ni has a strong effect in decreasing the C solubility, there is no discernible effect of Ni on C solubility in S-rich Fe-Ni alloy liquids. Furthermore, we also find that $D_C^{alloy/silicate}$ significantly decreases with increasing S content in the alloy liquid from ~11 wt% to ~24 wt% S in the alloy. Our data have important implications for core-mantle fractionation of carbon in terrestrial bodies such as Earth and Mars as well as various small planetary embryos that likely acted as building blocks in late stage growth of proto-Earth. We show that for equilibrium core formation scenarios, planets such as Mars, with a sulfur-rich metallic core, could obtain a relatively more carbon-rich silicate magma ocean compared to that for the Earth, which is thought to have an S-poor core. Hence if both Earth and Mars differentiated via an equilibrium alloy-silicate fractionation and if both bodies had similar carbon budget that participated in core formation, Martian bulk silicate reservoir would be more carbon rich than that of the BSE. In this case, however, the resulting BSE would be 1–2 orders of magnitude lower in carbon compared to the estimate in the present-day mantle of the Earth. Protracted growth of the proto-Earth through late stage impacts of large differentiated embryos could, however, have had created the opportunity for the Earth to acquire its silicate fraction's carbon budget. Calculations, based on our new partitioning and solubility data validate the previous model of Li et al. (2016a) where the BSE carbon and sulfur budget can be established via disequilibrium merger of an S-rich differentiated impactor. Our new experiments show that the impactor which can be 9–20% the mass of the Earth, needs to be more enriched in the bulk carbon content than what was predicted by the model of Li et al. (2016a). This is owing to the fact that C solubility in S-rich alloy at high P-T is higher than the lower pressure estimates used in the study of Li et al. (2016a).

ACKNOWLEDGMENTS

The authors thank Gelu Costin for his assistance on the electron probe, Ben Cerjan and Bob Zheng for their help on the aluminum coating, and Brian Monteleone for the SIMS analysis. Ali Bouhifd and two anonymous reviewers are thanked for their thorough, critical comments, which helped us improve the clarity of our communication. This work received support from NASA grant NNX13AM51G, a Packard Fellowship for Science and Engineering, and the Deep Carbon Observatory.

REFERENCES

Allègre C. J., Poirier J.-P., Humler E. and Hofmann A. W. (1995) The chemical composition of the Earth. *Earth Planet. Sci. Lett.* **134**, 515–526.

Armstrong L. S., Hirschmann M. M., Stanley B. D., Falksen E. G. and Jacobsen S. D. (2015) Speciation and solubility of reduced C-O–H–N volatiles in mafic melt: Implications for volcanism, atmospheric evolution, and deep volatile cycles in the terrestrial planets. *Geochim. Cosmochim. Acta* **171**, 283–302.

Badro J., Cote A. S. and Brodholt J. P. (2014) A seismologically consistent compositional model of Earth's core. *Proc. Natl. Acad. Sci.* **111**, 7542–7545.

Badro J., Brodholt J. P., Piet H., Siebert J. and Ryerson F. J. (2015) Core formation and core composition from coupled

geochemical and geophysical constraints. *Proc. Natl. Acad. Sci.* **112**, 12310–12314.
Bottke W. F., Nesvorný D., Grimm R. E., Morbidelli A. and O'Brien D. P. (2006) Iron meteorites as remnants of planetesimals formed in the terrestrial planet region. *Nature* **439**, 821–824.
Bouchard D. and Bale C. W. (1995) Simultaneous optimization of thermochemicai data for liquid iron alloys containing C, N, Ti, Si, Mn, S, and P. *Metall. Mater. Trans. B* **26B**, 467–484.
Bouhifd M. A. and Jephcoat A. P. (2011) Convergence of Ni and Co metal-silicate partition coefficients in the deep magma-ocean and coupled silicon-oxygen solubility in iron melts at high pressures. *Earth Planet. Sci. Lett.* **307**, 341–348.
Boujibar A., Andrault D., Bouhifd M. A., Bolfan-Casanova N., Devidal J. L. and Trcera N. (2014) Metal-silicate partitioning of sulphur, new experimental and thermodynamic constraints on planetary accretion. *Earth Planet. Sci. Lett.* **391**, 42–54.
Buono A. S., Dasgupta R., Lee C. T. A. and Walker D. (2013) Siderophile element partitioning between cohenite and liquid in the Fe-Ni-S-C system and implications for geochemistry of planetary cores and mantles. *Geochim. Cosmochim. Acta* **120**, 239–250.
Chen B., Li Z., Zhang D., Liu J., Hu M. Y., Zhao J., Bi W., Alp E. E., Xiao Y., Chow P. and Li J. (2014) Hidden carbon in Earth's inner core revealed by shear softening in dense Fe_7C_3. *Proc. Natl. Acad. Sci. USA* **111**, 17755–17758.
Chi H., Dasgupta R., Duncan M. S. and Shimizu N. (2014) Partitioning of carbon between Fe-rich alloy melt and silicate melt in a magma ocean – implications for the abundance and origin of volatiles in Earth, Mars, and the Moon. *Geochim. Cosmochim. Acta* **139**, 447–471.
Clesi V., Bouhifd M. A., Bolfan-Casanova N., Manthilake G., Fabbrizio A. and Andrault D. (2016) Effect of H_2O on metal-milicate partitioning of Ni Co, V, Cr, Mn and Fe: implications for the oxidation state of the Earth and Mars. *Geochim. Cosmochim. Acta* **192**, 97–121.
Clesi V., Bouhifd M. A., Bolfan-Casanova N., Manthilake G., Schiavi F., Raepsaet C., Bureau H., Khodja H. and Andrault D. (2018) Low hydrogen contents in the cores of terrestrial planets. *Sci. Adv.* **4**.
Corgne A., Siebert J. and Badro J. (2009) Oxygen as a light element: a solution to single-stage core formation. *Earth Planet. Sci. Lett.* **288**, 108–114.
Dalou C., Hirschmann M. M., von der Handt A., Mosenfelder J. and Armstrong L. S. (2017) Nitrogen and carbon fractionation during core–mantle differentiation at shallow depth. *Earth Planet. Sci. Lett.* **458**, 141–151.
Dasgupta R. (2013) Ingassing, storage, and outgassing of terrestrial carbon through geologic time. *Rev. Mineral. Geochem.* **75**, 183–229.
Dasgupta R. (2018) Volatile-bearing partial melts beneath oceans and continents – where, how much, and of what compositions? *Am. J. Sci.* **318**, 141–165.
Dasgupta R. and Hirschmann M. M. (2010) The deep carbon cycle and melting in Earth's interior. *Earth Planet. Sci. Lett.* **298**, 1–13.
Dasgupta R. and Walker D. (2008) Carbon solubility in core melts in a shallow magma ocean environment and distribution of carbon between the Earth's core and the mantle. *Geochim. Cosmochim. Acta* **72**, 4627–4641.
Dasgupta R., Buono A., Whelan G. and Walker D. (2009) High-pressure melting relations in Fe-C-S systems: implications for formation, evolution, and structure of metallic cores in planetary bodies. *Geochim. Cosmochim. Acta* **73**, 6678–6691.
Dasgupta R., Chi H., Shimizu N., Buono A. S. and Walker D. (2013) Carbon solution and partitioning between metallic and silicate melts in a shallow magma ocean: implications for the origin and distribution of terrestrial carbon. *Geochim. Cosmochim. Acta* **102**, 191–212.
Dauphas N. (2017) The isotopic nature of the Earth's accreting material through time. *Nature* **541**, 521–524.
Deguen R., Landeau M. and Olson P. (2014) Turbulent metal-silicate mixing, fragmentation, and equilibration in magma oceans. *Earth Planet. Sci. Lett.* **391**, 274–287.
Deng L., Fei Y., Liu X., Gong Z. and Shahar A. (2013) Effect of carbon, sulfur and silicon on iron melting at high pressure: implications for composition and evolution of the planetary terrestrial cores. *Geochim. Cosmochim. Acta* **114**, 220–233.
Ding S. and Dasgupta R. (2017) The fate of sulfide during decompression melting of peridotite – implications for sulfur inventory of the MORB-source depleted upper mantle. *Earth Planet. Sci. Lett.* **459**, 183–195.
Ding S., Dasgupta R., Lee C. T. A. and Wadhwa M. (2015) New bulk sulfur measurements of Martian meteorites and modeling the fate of sulfur during melting and crystallization – implications for sulfur transfer from Martian mantle to crust-atmosphere system. *Earth Planet. Sci. Lett.* **409**, 157–167.
Dreibus G. and Palme H. (1996) Cosmochemical constraints on the sulfur content in the Earth's core. *Geochim. Cosmochim. Acta* **60**, 1125–1130.
Duncan M. S. and Dasgupta R. (2017) Rise of Earth's atmospheric oxygen controlled by efficient subduction of organic carbon. *Nat. Geosci.* **10**, 387–392.
Duncan M. S., Dasgupta R. and Tsuno K. (2017) Experimental determination of CO_2 content at graphite saturation along a natural basalt-peridotite melt join: implications for the fate of carbon in terrestrial magma oceans. *Earth Planet. Sci. Lett.* **466**, 115–128.
Eggler D. H. (1978) The effect of CO_2 upon partial melting of peridotite in the system Na_2O–CaO–Al_2O_3–MgO–SiO_2–CO_2 to 35 kb, with an analysis of melting in a peridotite–H_2O–CO_2 system. *Am. J. Sci.*, 305–343.
Fei Y. and Brosh E. (2014) Experimental study and thermodynamic calculations of phase relations in the Fe–C system at high pressure. *Earth Planet. Sci. Lett.* **408**, 155–162.
Fischer R. A., Nakajima Y., Campbell A. J., Frost D. J., Harries D., Langenhorst F., Miyajima N., Pollok K. and Rubie D. C. (2015) High pressure metal-silicate partitioning of Ni Co, V, Cr, Si, and O. *Geochim. Cosmochim. Acta* **167**, 177–194.
Frost D. J. and Dolejš D. (2007) Experimental determination of the effect of H_2O on the 410-km seismic discontinuity. *Earth Planet. Sci. Lett.* **256**, 182–195.
Gross J., Filiberto J. and Bell A. S. (2013) Water in the martian interior: evidence for terrestrial MORB mantle-like volatile contents from hydroxyl-rich apatite in olivine-phyric shergottite NWA 6234. *Earth Planet. Sci. Lett.* **369–370**, 120–128.
Halevy I., Zuber M. T. and Schrag D. P. (2007) A sulfur dioxide climate feedback on Early Mars. *Science* **318**, 1903–1907.
Helo C., Longpré M.-A., Shimizu N., Clague D. a. and Stix J. (2011) Explosive eruptions at mid-ocean ridges driven by CO_2-rich magmas. *Nat. Geosci.* **4**, 260–263.
Hirayama Y., Fujii T. and Kurita K. (1993) The melting relation of the system, iron and carbon at high pressure and its bearing on the early stage of the earth. *Geophys. Res. Lett.* **20**, 2095–2098.
Hirschmann M. M. (2016) Constraints on the early delivery and fractionation of Earth's major volatiles from C/H, C/N, and C/S ratios. *Am. Mineral.* **101**, 540–553.
Hirschmann M. M. and Dasgupta R. (2009) The H/C ratios of Earth's near-surface and deep reservoirs, and consequences for deep Earth volatile cycles. *Chem. Geol.* **262**, 4–16.
Holzheid A., Palme H. and Chakraborty S. (1997) The activities of NiO, CoO and FeO in silicate melts. *Chem. Geol.* **139**, 21–38.

Javoy M., Kaminski E., Guyot F., Andrault D., Sanloup C., Moreira M., Labrosse S., Jambon A., Agrinier P., Davaille A. and Jaupart C. (2010) The chemical composition of the Earth: enstatite chondrite models. *Earth Planet. Sci. Lett.* **293**, 259–268.

Kegler Ph., Holzheid A., Frost D. J., Rubie D. C., Dohmen R. and Palme H. (2008) New Ni and Co metal-silicate partitioning data and their relevance for an early terrestrial magma ocean. *Earth Planet. Sci. Lett.* **268**, 28–40.

Kelemen P. B. and Manning C. E. (2015) Reevaluating carbon fluxes in subduction zones, what goes down, mostly comes up. *Proc. Natl. Acad. Sci.* **112**, E3997–E4006.

Kiseeva E. S. and Wood B. J. (2013) A simple model for chalcophile element partitioning between sulphide and silicate liquids with geochemical applications. *Earth Planet. Sci. Lett.* **383**, 68–81.

Kuramoto K. (1997) Accretion, core formation, H and C evolution of the Earth and Mars. *Phys. Earth Planet. Int.* **100**, 3–20.

Kuramoto K. and Matsui T. (1996) Partitioning of H and C between the mantle and core during the core formation in the Earth: Its implications for the atmospheric evolution and redox state of early mantle. *J. Geophys. Res.* **101**, 14909–14932.

Labidi J., Shahar A., Le Losq C., Hillgren V. J., Mysen B. O. and Farquhar J. (2016) Experimentally determined sulfur isotope fractionation between metal and silicate and implications for planetary differentiation. *Geochim. Cosmochim. Acta* **175**, 181–194.

Lee C.-T. A., Luffi P., Chin E. J., Bouchet R., Dasgupta R., Morton D. M., Le Roux V., Yin Q.-Z. and Jin D. (2012) Copper systematics in arc magmas and implications for crust-mantle differentiation. *Science* **336**, 64–68.

Le Voyer M., Kelley K. A., Cottrell E. and Hauri E. H. (2017) Heterogeneity in mantle carbon content from CO_2-undersaturated basalts. *Nat. Commun.* **8**, 14062. https://doi.org/10.1038/ncomms14062.

Li Y. and Audétat A. (2012) Partitioning of V, Mn Co, Ni, Cu, Zn, As, Mo, Ag, Sn, Sb, W, Au, Pb, and Bi between sulfide phases and hydrous basanite melt at upper mantle conditions. *Earth Planet. Sci. Lett.* **355–356**, 327–340.

Li Y., Dasgupta R. and Tsuno K. (2015) The effects of sulfur, silicon, water, and oxygen fugacity on carbon solubility and partitioning in Fe-rich alloy and silicate melt systems at 3 GPa and 1600 °C: implications for core–mantle differentiation and degassing of magma oceans and reduced planet. *Earth Planet. Sci. Lett.* **415**, 54–66.

Li Y., Dasgupta R. and Tsuno K. (2017) Carbon contents in reduced basalts at graphite saturation: implications for the degassing of Mars, Mercury, and the Moon. *J. Geophys. Res. Planets* **122**. https://doi.org/10.1002/2017JE005289.

Li Y., Dasgupta R., Tsuno K., Monteleone B. and Shimizu N. (2016a) Carbon and sulfur budget of the silicate Earth explained by accretion of differentiated planetary embryos. *Nat. Geosci.* **9**, 781–785.

Li Y., Marty B., Shcheka S., Zimmermann L. and Keppler H. (2016b) Nitrogen isotope fractionation during terrestrial core-mantle separation. *Geochem. Perspect. Lett.* **2**, 138–147.

Lodders K. and Fegley B. (1997) An oxygen isotope model for the composition of mars. *Icarus* **126**, 373–394.

Ma Z. (2001) Thermodynamic description for concentrated metallic solutions using interaction parameters. *Metall. Mater. Trans. B* **32**, 87–103.

Mallik A. and Dasgupta R. (2014) Effect of variable CO_2 on eclogite-derived andesite and lherzolite reaction at 3 GPa—implications formantle source characteristics of alkalic ocean island basalts. *Geochem.Geophys. Geosyst.* **15**, 1533–1557.

Marty B. (2012) The origins and concentrations of water, carbon, nitrogen and noble gases on Earth. *Earth Planet. Sci. Lett.* **313–314**, 56–66.

McCubbin F. M., Smirnov A., Nekvasil H., Wang J., Hauri E. and Lindsley D. H. (2010) Hydrous magmatism on Mars: a source of water for the surface and subsurface during the Amazonian. *Earth Planet. Sci. Lett.* **292**, 132–138.

McCubbin F. M., Hauri E. H., Elardo S. M., Vander Kaaden K. E., Wang J. and Shearer C. K. (2012) Hydrous melting of the martian mantle produced both depleted and enriched shergottites. *Geology* **40**, 683–686.

McDonough W. F. (2013) Compositional model for the earth's core. *Treatise Geochem. Second Ed.* **3**, 559–577.

McDonough W. F. and Sun S. S. (1995) The Composition of the Earth. *Chem. Geol.* **120**, 223–253.

Michael P. J. and Graham D. W. (2015) The behavior and concentration of CO_2 in the suboceanic mantle: inferences from undegassed ocean ridge and ocean island basalts. *Lithos* **236–237**, 338–351.

Morgan J. W. and Anders E. (1979) Chemical composition of Mars. *Geochim. Cosmochim. Acta* **43**, 1601–1610.

Nakajima Y., Takahashi E., Suzuki T. and Funakoshi K. (2009) "Carbon in the core" revisited. *Phys. Earth Planet. Inter.* **174**, 202–211.

Nakajima Y., Imada S., Hirose K., Komabayashi T., Ozawa H. and Tateno S. (2015) Carbon-depleted outer core revealed by sound velocity measurements of liquid iron–carbon alloy. *Nat. Commun.* **6**. https://doi.org/10.1038/ncomms9942.

Namur O., Charlier B., Holtz F., Cartier C. and McCammon C. (2016) Sulfur solubility in reduced mafic silicate melts: Implications for the speciation and distribution of sulfur on Mercury. *Earth Planet. Sci. Lett.* **448**, 102–114.

Nickel K. G., Brey G. P. and Kogarko L. (1985) Orthopyroxene-clinopyroxene equilibria in the system CaO-MgO-Al_2O_3-SiO_2 (CMAS) – new experimental results and implications for 2-pyroxene thermometry. *Contrib. Mineral. Petrol.* **91**, 44–53.

O'Brien D. P., Walsh K. J., Morbidelli A., Raymond S. N. and Mandell A. M. (2014) Water delivery and giant impacts in the "Grand Tack" scenario. *Icarus* **239**, 74–84.

O'Neill H. S. C. (1991) The origin of the Moon and the early history of the Earth – a chemical model. Part 1: The Moon. *Geochim. Cosmochim. Acta* **55**, 1135–1157.

O'Neill H. S. C. and Eggins S. M. (2002) The effect of melt composition on trace element partitioning: an experimental investigation of the activity coefficients of FeO, NiO, CoO, MoO_2 and MoO_3 in silicate melts. *Chem. Geol.* **186**, 151–181.

Ono S., Kikegawa T., Higo Y. and Tange Y. (2017) Precise determination of the phase boundary between coesite and stishovite in SiO_2. *Phys. Earth Planet. Int.* **264**, 1–6.

Palme H. and O'Neill H. (2013) Cosmochemical estimates of mantle composition. *Treatise Geochem. Second Ed.* **3**, 1–39.

Pearson V. K., Sephton M. A., Franchi I. A., Gibson J. M. and Gilmour I. (2006) Carbon and nitrogen in carbonaceous chondrites: elemental abundances and stable isotopic compositions. *Meteorit. Planet. Sci.* **41**, 1899–1918.

Prescher C., Dubrovinsky L., Bykova E., Kupenko I., Glazyrin K., Kantor A., McCammon C., Mookherjee M., Nakajima Y., Miyajima N., Sinmyo R., Cerantola V., Dubrovinskaia N., Prakapenka V., Rüffer R., Chumakov A. and Hanfland M. (2015) High Poisson's ratio of Earth's inner core explained by carbon alloying. *Nat. Geosci.* **8**, 220–223.

Rai N. and Van Westrenen W. (2013) Core-mantle differentiation in Mars. *J. Geophys. Res. Planets* **118**, 1195–1203.

Righter K. (2011) Prediction of metal-silicate partition coefficients for siderophile elements: an update and assessment of PT

conditions for metal-silicate equilibrium during accretion of the Earth. *Earth Planet. Sci. Lett.* **304**, 158–167.

Righter K. and Chabot N. L. (2011) Moderately and slightly siderophile element constraints on the depth and extent of melting in early Mars. *Meteorit. Planet. Sci.* **46**, 157–176.

Rubie D. C., Frost D. J., Mann U., Asahara Y., Nimmo F., Tsuno K., Kegler P., Holzheid A. and Palme H. (2011) Heterogeneous accretion, composition and core–mantle differentiation of the Earth. *Earth Planet. Sci. Lett.* **301**, 31–42.

Rubie D. C., Jacobson S. A., Morbidelli A., O'Brien D. P., Young E. D., de Vries J., Nimmo F., Palme H. and Frost D. J. (2015) Accretion and differentiation of the terrestrial planets with implications for the compositions of early-formed Solar System bodies and accretion of water. *Icarus* **248**, 89–108.

Sanloup C., Jambon A. and Gillet P. (1999) A simple chondrite model of Mars. *Phys. Earth Planet. Int.* **112**, 43–54.

Sanloup C., van Westrenen W., Dasgupta R., Maynard-Casely H. and Perrillat J. P. (2011) Compressibility change in iron-rich melt and implications for core formation models. *Earth Planet. Sci. Lett.* **306**, 118–122.

Sarafian A. R., Nielsen S. G., Marschall H. R., McCubbin F. M. and Monteleone B. D. (2014) Early accretion of water in the inner solar system from a carbonaceous chondrite-like source. *Science* **346**, 623–626.

Siebert J., Badro J., Antonangeli D. and Ryerson F. (2013) Terrestrial accretion under oxidising conditions. *Science* **339**, 1194–1198.

Stanley B. D., Hirschmann M. M. and Withers A. C. (2014) Solubility of C–O–H volatiles in graphite-saturated martian basalts. *Geochim. Cosmochim. Acta* **129**, 54–76.

Suer T.-A., Siebert J., Remusat L., Menguy N. and Fiquet G. (2017) A sulfur-poor terrestrial core inferred from metal–silicate partitioning experiments. *Earth Planet. Sci. Lett.* **469**, 84–97.

Tsuno K. and Dasgupta R. (2015) Fe–Ni–Cu–C–S phase relations at high pressures and temperatures – the role of sulfur in carbon storage and diamond stability at mid- to deep-upper mantle. *Earth Planet. Sci. Lett.* **412**, 132–142.

Tsymbulov L. B. and Tsemekhman L. S. (2001) Solubility of carbon in sulfide melts of the system Fe-Ni-S. *Russ. J. Appl. Chem.* **74**, 925–929.

Tuff J., Wood B. J. and Wade J. (2011) The effect of Si on metal–silicate partitioning of siderophile elements and implications for the conditions of core formation. *Geochim. Cosmochim. Acta* **75**, 673–690.

Urakawa S., Someya K., Terasaki H., Katsura T., Yokoshi S., Funakoshi K. Ich, Utsumi W., Katayama Y., Sueda Y. ichir and Irifune T. (2004) Phase relationships and equations of state for FeS at high pressures temperatures and implications for the internal structure of Mars. *Phys. Earth Planet. Int.* **143**, 469–479.

Wade J. and Wood B. J. (2005) Core formation and the oxidation state of the Earth. *Earth Planet. Sci. Lett.* **236**, 78–95.

Wade J. and Wood B. J. (2016) The oxidation state and mass of the Moon-forming impactor. *Earth Planet. Sci. Lett.* **442**, 186–193.

Wade J., Wood B. J. and Tuff J. (2012) Metal-silicate partitioning of Mo and W at high pressures and temperatures: evidence for late accretion of sulphur to the Earth. *Geochim. Cosmochim. Acta* **85**, 58–74.

Walker D., Dasgupta R., Li J. and Buono A. (2013) Nonstoichiometry and growth of some Fe carbides. *Contrib. Mineral. Petrol.* **166**, 935–957.

Walsh K. J., Morbidelli A., Raymond S. N., O'Brien D. P. and Mandell A. M. (2012) A low mass for Mars from Jupiter's early gas-driven migration. *Nature* **475**, 206–209.

Walter M. J. and Cottrell E. (2013) Assessing uncertainty in geochemical models for core formation in Earth. *Earth Planet. Sci. Lett.* **365**, 165–176.

Wang Y., Wen L. and Weidner D. J. (2013) Composition of Mars constrained using geophysical observations and mineral physics modeling. *Phys. Earth Planet. Int.* **224**, 68–76.

Wang C., Hirama J., Nagasaka T. and Ban-Ya S. (1991) Phase equilibria of liquid Fe-S-C ternary system. *ISIJ Int.* **31**, 1292–1299.

Wasson J. and Kallemeyn G. (1998) Compositions of chondrites. *Philos. Trans. R. Soc. A* **325**, 535–544.

Wohlers A. and Wood B. J. (2015) A mercury-like component of early Earth yields uranium in the core and high mantle ^{142}Nd. *Nature* **520**, 337–340.

Wohlers A. and Wood B. J. (2017) Uranium, thorium and REE partitioning into sulfide liquids: implications for reduced S-rich bodies. *Geochim. Cosmochim. Acta* **205**, 226–244.

Wood B. J. (1993) Carbon in the core. *Earth Planet. Sci. Lett.* **117**, 593–607.

Wood B. J. (2008) Accretion and core formation: constraints from metal-silicate partitioning. *Philos. Trans. RSoc. A Math. Phys. Eng. Sci.* **366**, 4339–4355.

Wood B. J., Kiseeva E. S. and Mirolo F. J. (2014) Accretion and core formation: the effects of sulfur on metal-silicate partition coefficients. *Geochim. Cosmochim. Acta* **145**, 248–267.

Wood B. J., Li J. and Shahar A. (2013) Carbon in the core: its influence on the properties of core and mantle. *Rev. Mineral. Geochemistry* **75**, 231–250.

Wyllie P. J. and Huang W.-L. (1975) Influence of mantle CO_2 in the generation of carbonatites and kimberlites. *Nature* **257**, 297–299.

Zahnle K., Arndt N., Cockell C., Halliday A., Nisbet E., Selsis F. and Sleep N. H. (2007) Emergence of a habitable planet. *Space Sci. Rev.* **129**, 35–78.

Zhang J., Li B., Utsumi W. and Liebermann R. (1996) In situ X-ray observations of the coesite-stishovite transition: reversed phase boundary and kinetics. *Phys. Chem. Miner.* **23**, 1–10.

Zhang Z., Lentsch N. and Hirschmann M. M. (2015). *Contrib. Mineral Petr.* **170**, 47. https://doi.org/10.1007/s00410-015-1202-z.

Zhang Z., Hastings P., Von der Handt A. and Hirschmann M. M. (2018) Experimental determination of carbon solubility in Fe-Ni-S melts. *Geochim. Cosmochim. Acta* **225**, 66–79.

Associate editor: Munir Humayun